

1  
2  
3  
4  
5  
6 Serotonin transporter-ibogaine complexes illuminate mechanisms of inhibition and transport  
7  
8

9 Jonathan A. Coleman<sup>‡a</sup>, Dongxue Yang<sup>‡a</sup>, Zhiyu Zhao<sup>b</sup>, Po-Chao Wen<sup>b</sup>, Craig Yoshioka<sup>c</sup>, Emad  
10 Tajkhorshid<sup>b</sup>, and Eric Gouaux<sup>a,d</sup>

11  
12  
13 <sup>‡</sup> These authors contributed equally.

14 a. Vollum Institute, Oregon Health & Science University, Portland, Oregon 97239, USA.

15 b. Department of Biochemistry, NIH Center for Macromolecular Modeling and Bioinformatics,  
16 Center for Biophysics and Quantitative Biology, and Beckman Institute for Advanced Science  
17 and Technology, University of Illinois at Urbana-Champaign, 405 N. Mathews Ave., Urbana, IL  
18 61801, USA.

19 c. Department of Biomedical Engineering, Oregon Health and Science University, 2730 SW  
20 Moody Ave, Portland, Oregon 97201, USA.

21 d. Howard Hughes Medical Institute, Oregon Health & Science University, Portland, Oregon  
22 97239, USA.

23  
24  
25 Correspondence to Eric Gouaux: [gouauxe@ohsu.edu](mailto:gouauxe@ohsu.edu)

26

27 **SUMMARY**

28 The serotonin transporter (SERT) regulates neurotransmitter homeostasis through the  
29 sodium-and chloride-dependent recycling of serotonin into presynaptic neurons<sup>1-3</sup>. Major  
30 depression and anxiety disorders are treated using selective serotonin reuptake  
31 inhibitors (SSRIs), small molecules that competitively block substrate binding,  
32 prolonging neurotransmitter action<sup>2,4</sup>. The dopamine and norepinephrine transporters,  
33 together with SERT, are members of the neurotransmitter sodium symporter (NSS) family.  
34 Cocaine and amphetamines inhibit or modulate the transport activities of NSSs<sup>2,3</sup> and  
35 genetic variants are associated with multiple neuropsychiatric disorders including  
36 attention deficit hyperactivity disorder, autism, and bipolar disorder<sup>2,5</sup>. Studies of  
37 bacterial NSS homologs, including LeuT, have shown how transmembrane helices (TMs)  
38 undergo conformational changes during the transport cycle, exposing a central binding  
39 site to either side of the membrane<sup>1,6-12</sup>. However, the conformational changes associated  
40 with transport in eukaryotic NSSs remain obscure. To elucidate structure-based  
41 mechanisms for transport in SERT, we turned to complexes with ibogaine, a centuries  
42 old hallucinogenic natural product with psychoactive and anti-addictive properties<sup>13,14</sup>  
43 (Fig. 1a). Interestingly, ibogaine displays non-competitive inhibition of transport, yet it  
44 exhibits competitive binding toward SSRIs<sup>15,16</sup>. Here we report cryo-EM structures of  
45 SERT-ibogaine complexes captured in outward-open, occluded, and inward-open  
46 conformations. Ibogaine binds to the central binding site and closure of the extracellular  
47 gate largely involves movements of TMs 1b and 6a. Opening of the intracellular gate  
48 involves a hinge-like movement of TM1a and partial unwinding of TM5, which together  
49 create a permeation pathway enabling substrate and ion diffusion to the cytoplasm.  
50 These structures define the structural rearrangements that occur from outward-open to  
51 the inward-open conformations, providing insight into the mechanism of  
52 neurotransmitter transport and ibogaine inhibition.

53

54 **MAIN TEXT**

55 SERT, a ~70 kDa monomeric membrane protein, poses a challenge for single particle  
56 cryo-EM, and thus we used antibody fragments to provide mass and molecular features to  
57 facilitate cryo-EM reconstruction<sup>17</sup>. We also employed a N- and C-terminally truncated SERT  
58 construct, deemed  $\Delta$ N72,C13, as well as three thermostable variants: ts2-active SERT, which  
59 maintains wild-type-like transport properties; ts2-inactive SERT<sup>18</sup> which is locked in the outward-  
60 open conformation; and C7x, which is devoid of reactive cysteines<sup>19</sup>. To interrogate ibogaine  
61 modulation of SERT, we determined ibogaine inhibition of serotonin uptake for the ts2-active  
62 and  $\Delta$ N72,C13 variants, finding that the  $IC_{50}$  is  $5 \pm 1 \mu\text{M}$  (Extended Data Fig. 1a). Upon addition  
63 of  $5 \mu\text{M}$  ibogaine, the  $V_{\text{max}}$  was reduced by approximately 50% and the  $K_m$  for serotonin was  
64 unchanged (Extended Data Fig. 1b), consistent with ibogaine acting as a non-competitive  
65 inhibitor<sup>16</sup>. We also investigated the consequences of antibody binding, demonstrating that the  
66 ts2-active 15B8 Fab/8B6 scFv complex is transport inactive (Fig. 1b) while the  $\Delta$ N72,C13  
67 SERT-15B8 Fab complex is transport competent (Fig. 1b).

68 Saturation binding experiments of [<sup>3</sup>H]ibogaine in NaCl to ts2-active SERT without or  
69 with the 15B8 Fab yielded  $K_d$  values of  $400 \pm 100 \text{ nM}$  and  $500 \pm 200 \text{ nM}$  (Fig. 1c), respectively.  
70 To investigate if ibogaine can also bind to the outward-open conformation, we carried out  
71 binding experiments on two variants locked in the outward-open conformation. Via direct binding  
72 experiments of [<sup>3</sup>H]ibogaine to the ts2-active 15B8 Fab/8B6 scFv complex and the ts2-inactive  
73 variant, we estimate a  $K_d$  of  $5\text{-}8 \mu\text{M}$  while in [<sup>3</sup>H]paroxetine competition experiments with the ts2-  
74 active 15B8 Fab/8B6 scFv complex we measured a  $K_i$  of  $3 \pm 0.4 \mu\text{M}$  (Extended Data Fig. 1c,d),  
75 experiments which together demonstrate that ibogaine binds ~10-fold more weakly to the  
76 outward-open conformation. Moreover, electrophysiological recordings demonstrate that the  
77 ibogaine binding site is accessible from the extracellular solution<sup>15,20</sup>, reinforcing the notion that  
78 ibogaine can bind to the transporter by way of the outward-open conformation. We further

79 explored ion dependence and found that ibogaine binds to SERT more tightly in KCl ( $K_d$  of 130  
80  $\pm 30$  nM) or *N*-methyl-D-glucamine hydrochloride (NMDG-Cl;  $K_d$  of 140  $\pm 20$  nM) than in NaCl, in  
81 agreement with prior studies<sup>21</sup>, and that the 15B8 Fab does not perturb ibogaine binding in KCl (  $K_d$   
82 of 180  $\pm 50$  nM) (Fig. 1c).

83 To probe the conformation of SERT employed in the cryo-EM studies reported here, we  
84 examined the Ser277Cys mutant, a residue located in the intracellular portion of TM5 that is  
85 solvent accessible in the inward-open conformation<sup>15,16,19,22,23</sup> (Extended Data Fig 1e). As  
86 reported previously<sup>15,16</sup>, the Ser277Cys mutant in the C7x background, when bound to ibogaine,  
87 is more reactive to methanethiosulfonate reagents than when bound to inhibitors that stabilize  
88 the outward-open conformation (Extended Data Fig. 1f,g); this differential reactivity of the  
89 Ser277Cys variant is further pronounced in KCl in comparison to NaCl (Fig. 1d). Taken together,  
90 these observations are consistent with the notion that ibogaine increases the accessibility of the  
91 cytoplasmic permeation pathway.

92 To understand where ibogaine binds to SERT and how ibogaine binding influences the  
93 conformation of the transporter, we studied SERT using single particle cryo-EM. To first validate  
94 that such studies were feasible, we carried out a ‘control’ reconstruction using the ts2-inactive  
95 15B8 Fab/8B6 scFv complex with the SSRI, paroxetine. We discovered that the cryo-EM map is  
96 well fit by the x-ray structure of the ts2-inactive, outward-open paroxetine complex (Extended  
97 Data Table 1), and that the map has clear density features for aromatic side-chains and for  
98 paroxetine in the central binding site, thus demonstrating the feasibility of single particle cryo-  
99 EM of SERT-antibody complexes (Extended Data Fig. 1h-j, Extended Data Fig. 2). With the  
100 feasibility of single particle studies established, we employed the ts2-active SERT-15B8  
101 Fab/8B6 scFv complex to investigate ibogaine binding to the outward-open conformation. This  
102 ibogaine-bound complex was determined at a resolution of  $\sim$ 4.1 Å (Fig. 2a, Extended Data  
103 Table 1). The TM densities were well-defined, continuous and of sufficient strength and  
104 connectivity to fit the main chain and to position many of the side chains (Extended Data Fig.

105 3a-g). Comparison of this complex with known structures of SERT and other transporters  
106 allowed unambiguous assignment as the outward-open conformation (Extended Data Fig 3g-i,  
107 Extended Data Table 1).

108 To further explore the conformations of SERT-ibogaine complexes, we employed Fabs  
109 that preserve uptake activity, first elucidating the structure of the  $\Delta$ N72,C13 SERT-15B8 Fab  
110 complex in NaCl, obtaining a reconstruction of the complex at  $\sim$ 4.2 Å, revealing a conformation  
111 distinct from the outward-open (Extended Data Fig. 4, Extended Data Table 1). Adjacent to  
112 TM1a, a density feature was found that is fit well by a molecule of cholesteryl hemisuccinate  
113 (CHS), similar to that observed in the dopamine transporter<sup>24,25</sup> (Fig. 2b). Comparison of the  
114 positions of TM1 and 6 and the extracellular gate to the equivalent elements of the outward-  
115 open complex indicates that this SERT-15B8 Fab-ibogaine complex, in NaCl, adopts an  
116 occluded conformation (Fig. 2b, Extended Data Fig. 4h).

117 In the presence of sodium, the accessibility of residues in the cytoplasmic permeation  
118 pathway is reduced<sup>19</sup>, showing that these conditions populate the inward-closed conformation  
119 while removal of sodium increases Thr276 phosphorylation<sup>23</sup> and favors the inward-open  
120 conformation (Fig. 1d). Thus, we examined the conformation of the  $\Delta$ N72,C13 SERT-15B8 Fab-  
121 ibogaine complex in KCl; the resulting reconstruction yielded a density map at a resolution of  
122  $\sim$ 3.6 Å (Fig. 2c, Extended Data Fig. 5, Extended Data Table 1, Supplementary Video 1). At the  
123 cytoplasmic side, a distinct density feature associated with TM1a was observed in this  
124 reconstruction, corresponding to a ‘splayed’ conformation of TM1a away from the transporter  
125 core, opening the intracellular pathway. The density feature for CHS near TM1a in the occluded  
126 conformation (Extended Data Fig. 6a) was not observed in the inward conformation, suggesting  
127 that its association may be conformation-dependent. Removal of cholesterol from membranes  
128 increases ibogaine binding and mutation of residues lining the CHS binding site favors the  
129 inward conformation<sup>26</sup>. Non-proteinaceous features were also found near Thr276 and Ser277,  
130 sites of phosphorylation that influence transporter conformational equilibria<sup>23</sup> (Extended Data

131 Fig. 6b). To further explore the influence of small molecules on the conformation of SERT, we  
132 examined noribogaine, an ibogaine metabolite<sup>27</sup> and non-competitive inhibitor of serotonin  
133 uptake (Fig. 1a, Extended Data Fig. 6c-e). A 3D reconstruction of the ΔN72,C13 SERT-15B8  
134 Fab complex with noribogaine in 100 mM KCl yielded a density map at 6.3 Å, allowing  
135 visualization of helical segments (Extended Data Table 1). Subsequent rigid-body fitting of  
136 outward-open, occluded or the inward-open conformations into the density map showed that the  
137 best fit was obtained with inward-open (Extended Data Fig. 6f-h), demonstrating that in KCl,  
138 ibogaine and noribogaine populate the inward-open conformation.

139 The quality of the density maps allowed localization of ibogaine at the central site and no  
140 other density features attributable to ibogaine. Because the density maps are between 3.6-4.2 Å  
141 resolution, however, we employed computational docking followed by molecular dynamics  
142 simulations to determine the optimal binding poses of ibogaine in the central site (Fig. 3a-c,  
143 Extended Data Fig. 7, Supplementary Video 2). We discovered that the tertiary amine of  
144 ibogaine interacts with Asp98 (Fig 3a,b, Extended Data Fig. 7b) while the tricyclic ring system  
145 lodges between the aromatic groups of Tyr176 and Tyr95 in the outward-open and occluded  
146 conformations. SERT-ibogaine interactions which are largely preserved in all three  
147 conformations include: the methoxy- group of ibogaine which protrudes into a cavity between  
148 TM3 and TM8, near Asn177; Ile172 which sits ‘above’ the tryptamine group and restrains the  
149 drug within the central site; and the aromatic ring of Phe341 which is adjacent to the indole  
150 nitrogen. Phe335 undergoes conformational changes in going from outward-open and occluded  
151 to the inward-open conformation where it moves further into the central site, ultimately blocking  
152 ibogaine release from the extracellular side (Fig 3a-c; Supplementary Video 3), while the  
153 movement of TM1a in the inward-open conformation disrupts interactions of Tyr95 and Asp98  
154 with ibogaine (Fig 3c). Thus, upon transition of the transporter from outward-open to inward-  
155 open, the position of ibogaine adjusts in the direction of TM1a and TM8 toward the cytoplasmic  
156 permeation pathway (Fig 3d, Supplementary Video 3).

157       Upon assessing the binding pose of ibogaine, we observed that the side chain of Asn177  
158    resides near the methoxy group of ibogaine and we reasoned that if the pose is accurate,  
159    mutation of the Asn to a smaller, less polar residue should enhance and diminish ibogaine and  
160    noribogaine affinity, respectively. We thus measured the inhibition of transport by ibogaine and  
161    noribogaine and also the binding of [<sup>3</sup>H]ibogaine for the Asn177Val, Asn177Ala, Asn177Thr and  
162    Asn177Leu mutants, finding more robust inhibition of 5-HT uptake by ibogaine and a weakening  
163    of inhibition by noribogaine (Fig. 3e, Extended Data Fig.8a). Strikingly, the Asn177Val variant  
164    has a substantially higher binding affinity for [<sup>3</sup>H]-ibogaine ( $70 \pm 20$  nM,  $P < 0.01$ , one-sided  
165    student's *t*-test) in KCl, additionally supporting the binding pose for ibogaine.

166       We next analyzed the position of the extracellular and intracellular gates to further define  
167    the conformation of SERT, finding that the ibogaine-bound, outward-open reconstruction is  
168    similar to the x-ray structure of paroxetine-bound SERT<sup>28</sup> (Extended Data Fig. 8b). Ibogaine and  
169    ions can access the central binding site from the extracellular side, because gating residues  
170    (Arg104-Glu493, C $\alpha$ -C $\alpha$  distance: 12.0 Å; Tyr176-Phe335: 13.6 Å), conform to an open gate  
171    (Fig. 3g) while the closed intracellular gate prevents exposure to the cytoplasm. Upon formation  
172    of the occluded conformation, SERT undergoes movements within the core TMs closing the  
173    extracellular gate, preventing access of the central binding site. In addition to the closure of the  
174    extracellular gate, the most substantial structural changes which occur during the transition from  
175    outward-open to the occluded conformation are found in TMs 1b, 5, 6, 7, 10 and in EL6  
176    (Extended Data Fig. 8c). The changes in helical position associated with TM6a include a tilting  
177    of 3° and a shift of 1.9 Å toward the scaffold. EL6 also moves by 1.3 Å toward TM1b and TM6a  
178    while TM10 tilts by 2° and shifts 0.9 Å in the same direction. TM7 shifts by 1.3 Å in the  
179    extracellular side toward the scaffold domain while TM5 experiences a 3.2° rotation and 1.3 Å  
180    shift toward TM7 and TM1b (Extended Data Fig. 8c-e). In NSSs, an allosteric site formed by  
181    residues in an extracellular vestibule modulates dissociation from the central site<sup>28-30</sup>. The  
182    closure of the extracellular gate (Arg104-Glu493: 9.7 Å; Tyr176-Phe335: 13.5 Å) changes the

183 nature of the extracellular vestibule, as the movement of TM6a toward the scaffold results in the  
184 collapse of the allosteric site as evidenced by a reduction in the solvent accessible surface area  
185 (SASA) (1448 vs. 1247 Å<sup>2</sup>), thus reducing the likelihood of association of ibogaine or similar  
186 small molecules to the allosteric site (Fig. 3g,h). EL3, which connects TM5 to TM6, further packs  
187 against the extracellular halves of these TMs. Subtle changes are also observed in EL4 which  
188 experiences a minor shift toward the scaffold, and localized changes in the intracellular portion  
189 of TM5 were observed, which may facilitate the transition to the inward-open conformation and  
190 opening of TM1a (Fig 3h).

191 We also investigated the conformational transitions from the occluded to the inward-  
192 open states, finding that the most noteworthy structural rearrangements are at the closed  
193 extracellular and open intracellular gates. TM1b shifts and tilts by 5.1 Å and 22° while TM6a  
194 moves by 3.4 Å and 5° further toward the scaffold, closing the extracellular gate as evidenced  
195 by a further reduction in the SASA of the allosteric site (973 Å<sup>2</sup>) and the distance between  
196 extracellular gating residues (Arg104-Glu493: 9.9 Å; Tyr176-Phe335: 11.0 Å) (Fig. 3h,i,  
197 Extended Data Fig. 8c). TM2 and TM7 undergo an associated movement of 2.8 and 1.0 Å in the  
198 extracellular C $\alpha$  marker positions with an overall angular change of 7.3 and 4.8° toward the  
199 scaffold, respectively. A hinge-like movement of TM1a by 40° toward the plane of the membrane  
200 disrupts interactions between its N-terminus and the cytoplasmic half of TM6 (Tyr350, Trp82)  
201 that are present in the outward-open and occluded conformations (C $\alpha$ -C $\alpha$  distance: 7.0 Å in  
202 occluded), opening the cytoplasmic permeation pathway and granting cytoplasmic accessibility  
203 to the central binding site (Fig. 3g,i, Extended Data Fig. 8c-e). The movement of TM1a is  
204 accompanied by structural changes in TM5 which unwinds at the GlyX<sub>9</sub>Pro motif<sup>7</sup> and expands  
205 laterally into the membrane, facilitating a shift of 1.8 Å in the intracellular side and 1 Å in the  
206 extracellular side and an angular change of 7° (Fig. 3i, Extended Data Fig. 8f-h). The net result  
207 of these movements is a constriction of the extracellular surface and an expansion of the

208 intracellular diameter of the transporter as it transitions from occluded to inward-open (Extended  
209 Data Fig. 8c-h, Supplementary Video 4).

210 The movement of key helices against the scaffold domain mirrors the conformational  
211 changes observed in bacterial amino acid transporters, although deviations from the prototypical  
212 model are also present (Extended Data Fig. 9). The occluded conformation of SERT most  
213 closely resembles the outward-facing occluded conformation of LeuT<sup>11</sup> (Extended Data Fig. 9b).  
214 The inward-open conformation, the unwound region of TM5 and the degree of the extracellular  
215 gate closure most closely resembles MhsT while the open intracellular gate is reminiscent of  
216 inward-open LeuT (Extended Data Fig. 9c,e). In LeuT, EL4 undergoes a large-scale movement  
217 plugging the extracellular pathway (outward-open vs. inward-open RMSD 5.4 Å, Extended Data  
218 Fig. 9d). EL6 likely restricts EL4 in SERT, and more subtle adjustments of EL4 (outward-open  
219 vs. inward-open, RMSD 2.7 Å) were observed while changes in EL6 appear to be largely more  
220 critical for extracellular gate closure (outward-open vs. inward-open, RMSD 2.7 Å) (Extended  
221 Data Fig. 8h). Given the heterogeneity observed for TM1a in the MD simulations of LeuT<sup>10</sup>, it is  
222 possible that TM1a in SERT may also sample different orientations upon the rupture of the  
223 intracellular gate.

224 To gain insight into the occupancy of the sodium sites in the outward-open, occluded and  
225 inward-open conformations, we examined the conformations of the surrounding protein residues  
226 because, at the present resolutions, we are unable to resolve density for ions. In the outward-  
227 open and occluded conformations, the position of residues surrounding Na1 and Na2 sites  
228 suggest that these conformations are compatible with two bound sodium ions (Extended Data  
229 Fig. 10a). The shift of TM5 toward the membrane together with the unwinding of IL2 allows the  
230 cytoplasmic access of Na2 in the inward conformation (Fig. 3i, Extended Data Figs. 8f, 10b,c)  
231 similar to MhsT where the unwinding of TM5 at the GX<sub>9</sub>P motif is also thought to result in the  
232 release of sodium from the Na2 site<sup>7</sup>. Sodium coordinating residues at the Na1 site also  
233 undergo considerable displacement in the inward-open conformation but their arrangement

234 suggests that they may still be capable of ion binding. The arrangement of chloride coordinating  
235 residues is also consistent with an occupied  $\text{Cl}^-$  site which is not coupled to substrate flux<sup>31</sup>.  
236 Thus, the position of the ion sites suggest distinct roles of Na1, Na2, and for  $\text{Cl}^-$ , where Na2 may  
237 be directly coupled to substrate transport<sup>32</sup>.

238 We observe that ibogaine interacts with SERT in outward-open, occluded, and inward-  
239 open conformations and can be classified as an active site-binding inhibitor which displays non-  
240 competitive inhibition characteristics<sup>33</sup>. As ibogaine cannot directly access the central binding  
241 site in the occluded conformation, we speculate that ibogaine binds to either the outward-open  
242 or inward-open conformations, suggesting the possibility that it may remain bound and allow for  
243 transporter isomerization (Fig. 4). Binding of ibogaine to the inward conformation likely forms the  
244 basis for the non-competitive inhibition because serotonin does not compete for binding to this  
245 conformation and the SERT-ibogaine complex may exist in dynamic equilibrium with the  
246 occluded conformation, depending on the ionic conditions. Ibogaine binding in KCl is in accord  
247 with an isomechanistic mechanism<sup>33</sup> via direct binding to the inward-open conformation.  
248 However, the observation that there is an extracellularly accessible ibogaine binding site<sup>15,20</sup> is  
249 suggestive of a more complex two-step mechanism, where the first step involves binding to  
250 outward-open and the second step involves the stabilization of an occluded or inward-open<sup>33</sup>.  
251 The larger steric bulk of ibogaine, compared to serotonin, may preclude it from binding and  
252 unbinding from the central site through the intracellular pathway without considerable  
253 conformational fluctuation, even in the inward-open conformation, thus explaining why ibogaine  
254 is not a substrate (Extended Data Fig. 10b,c).

255 **REFERENCES**

256 1 Singh, S. K. & Pal, A. Biophysical approaches to the study of LeuT, a prokaryotic  
257 homolog of neurotransmitter sodium symporters. *Methods Enzymol* **557**, 167-198,  
258 (2015).  
259 2 Kristensen, A. S. et al. SLC6 neurotransmitter transporters: structure, function, and  
260 regulation. *Pharmacol Rev* **63**, 585-640, (2011).

261 3 Gether, U., Andersen, P. H., Larsson, O. M. & Schousboe, A. Neurotransmitter  
262 transporters: molecular function of important drug targets. *Trends Pharmacol Sci* **27**,  
263 375-383, (2006).

264 4 Cipriani, A. *et al.* Comparative efficacy and acceptability of 21 antidepressant drugs for  
265 the acute treatment of adults with major depressive disorder: a systematic review and  
266 network meta-analysis. *Lancet* **391**, 1357-1366, (2018).

267 5 Lin, Z. & Madras, B. K. Human genetics and pharmacology of neurotransmitter  
268 transporters. *Handb Exp Pharmacol*, 327-371, (2006).

269 6 Kazmier, K. *et al.* Conformational dynamics of ligand-dependent alternating access in  
270 LeuT. *Nat Struct Mol Biol* **21**, 472-479, (2014).

271 7 Malinauskaitė, L. *et al.* A mechanism for intracellular release of Na<sup>+</sup> by  
272 neurotransmitter/sodium symporters. *Nat Struct Mol Biol* **21**, 1006-1012, (2014).

273 8 Krishnamurthy, H. & Gouaux, E. X-ray structures of LeuT in substrate-free outward-open  
274 and apo inward-open states. *Nature* **481**, 469-474, (2012).

275 9 Merkle, P. S. *et al.* Substrate-modulated unwinding of transmembrane helices in the NSS  
276 transporter LeuT. *Sci Adv* **4**, eaar6179, (2018).

277 10 Grouleff, J., Sondergaard, S., Koldso, H. & Schiott, B. Properties of an inward-facing  
278 state of LeuT: conformational stability and substrate release. *Biophys J* **108**, 1390-1399,  
279 (2015).

280 11 Yamashita, A., Singh, S. K., Kawate, T., Jin, Y. & Gouaux, E. Crystal structure of a  
281 bacterial homologue of Na<sup>+</sup>/Cl<sup>-</sup>-dependent neurotransmitter transporters. *Nature* **437**,  
282 215-223, (2005).

283 12 Terry, D. S. *et al.* A partially-open inward-facing intermediate conformation of LeuT is  
284 associated with Na<sup>(+)</sup> release and substrate transport. *Nat Commun* **9**, 230, (2018).

285 13 Belgers, M. *et al.* Ibogaine and addiction in the animal model, a systematic review and  
286 meta-analysis. *Transl Psychiatry* **6**, e826, (2016).

287 14 Dybowski, J. L., E. PLANT CHEMISTRY. Concerning Iboga, its excitement-producing  
288 properties, its composition, and the new alkaloid it contains, ibogaine. *C. R. Acad. Sci.*  
289 **133**, 748, (1901).

290 15 Bulling, S. *et al.* The mechanistic basis for noncompetitive ibogaine inhibition of  
291 serotonin and dopamine transporters. *J Biol Chem* **287**, 18524-18534, (2012).

292 16 Jacobs, M. T., Zhang, Y. W., Campbell, S. D. & Rudnick, G. Ibogaine, a noncompetitive  
293 inhibitor of serotonin transport, acts by stabilizing the cytoplasm-facing state of the  
294 transporter. *J Biol Chem* **282**, 29441-29447, (2007).

295 17 Wu, S. *et al.* Fabs enable single particle cryoEM studies of small proteins. *Structure* **20**,  
296 582-592, (2012).

297 18 Coleman, J. A. & Gouaux, E. Structural basis for recognition of diverse antidepressants  
298 by the human serotonin transporter. *Nat Struct Mol Biol* **25**, 170-175, (2018).

299 19 Zhang, Y. W. & Rudnick, G. The cytoplasmic substrate permeation pathway of serotonin  
300 transporter. *J Biol Chem* **281**, 36213-36220, (2006).

301 20 Burtscher, V., Hotka, M., Li, Y., Freissmuth, M. & Sandtner, W. A label-free approach to  
302 detect ligand binding to cell surface proteins in real time. *Elife* **7**, (2018).

303 21 Tavouri, S., Forrest, L. R. & Rudnick, G. Fluoxetine (Prozac) binding to serotonin  
304 transporter is modulated by chloride and conformational changes. *J Neurosci* **29**, 9635-  
305 9643, (2009).

306 22 Ramamoorthy, S., Samuvel, D. J., Buck, E. R., Rudnick, G. & Jayanthi, L. D.  
307 Phosphorylation of threonine residue 276 is required for acute regulation of serotonin  
308 transporter by cyclic GMP. *J Biol Chem* **282**, 11639-11647, (2007).

309 23 Zhang, Y. W., Turk, B. E. & Rudnick, G. Control of serotonin transporter phosphorylation  
310 by conformational state. *Proc Natl Acad Sci U S A* **113**, E2776-2783, (2016).

311 24 Penmatsa, A., Wang, K. H. & Gouaux, E. X-ray structure of dopamine transporter  
312 elucidates antidepressant mechanism. *Nature* **503**, 85-90, (2013).

313 25 Wang, K. H., Penmatsa, A. & Gouaux, E. Neurotransmitter and psychostimulant  
314 recognition by the dopamine transporter. *Nature* **521**, 322-327, (2015).

315 26 Laursen, L. *et al.* Cholesterol binding to a conserved site modulates the conformation,  
316 pharmacology, and transport kinetics of the human serotonin transporter. *J Biol Chem*  
317 **293**, 3510-3523, (2018).

318 27 Mash, D. C., Staley, J. K., Baumann, M. H., Rothman, R. B. & Hearn, W. L. Identification  
319 of a primary metabolite of ibogaine that targets serotonin transporters and elevates  
320 serotonin. *Life Sci* **57**, PL45-50, (1995).

321 28 Coleman, J. A., Green, E. M. & Gouaux, E. X-ray structures and mechanism of the  
322 human serotonin transporter. *Nature* **532**, 334-339, (2016).

323 29 Chen, F. *et al.* Characterization of an allosteric citalopram-binding site at the serotonin  
324 transporter. *J Neurochem* **92**, 21-28, (2005).

325 30 Navratna, V., Tosh, D. K., Jacobson, K. A. & Gouaux, E. Thermostabilization and  
326 purification of the human dopamine transporter (hDAT) in an inhibitor and allosteric  
327 ligand bound conformation. *PLoS One* **13**, e0200085, (2018).

328 31 Hasenhuettl, P. S., Freissmuth, M. & Sandtner, W. Electrogenic Binding of Intracellular  
329 Cations Defines a Kinetic Decision Point in the Transport Cycle of the Human Serotonin  
330 Transporter. *J Biol Chem* **291**, 25864-25876, (2016).

331 32 Felts, B. *et al.* The two Na<sup>+</sup> sites in the human serotonin transporter play distinct roles in  
332 the ion coupling and electrogenicity of transport. *J Biol Chem* **289**, 1825-1840, (2014).

333 33 Blat, Y. Non-competitive inhibition by active site binders. *Chem Biol Drug Des* **75**, 535-  
334 540, (2010).

335

### 336 ENDNOTES

### 337 Acknowledgements

338 We thank the National Institute for Drug Abuse, Drug Supply Program for providing ibogaine and  
339 [<sup>3</sup>H]ibogaine. We thank L. Vaskalis for assistance with figures, H. Owen for help with manuscript  
340 preparation, and V. Navratna for helpful discussions. We thank M. Whorton for help with Fab x-  
341 ray data collection. Electron microscopy was performed at Oregon Health & Science University  
342 (OHSU) at the Multiscale Microscopy Core with technical support from the OHSU-FEI Living  
343 Lab and OHSU Center for Spatial Systems Biomedicine. We acknowledge the staff of the  
344 Northeastern Collaborative Access Team at the Advanced Photon Source. Simulations have  
345 been performed using NSF computing resources allocated through an XSEDE grant  
346 TGMCA06N060 to ET, and PRAC allocation (grant ACI1713784 to ET) at Blue Waters of the  
347 National Center for Supercomputing Applications at the University of Illinois. We are particularly

348 grateful to Bernard and Jennifer LaCroute for their generous support. This work was funded by  
349 the NIH (5R37MH070039 to E.G.; P41GM104601, U54GM087519 and R01GM123455 to E.T.).  
350 E.G. is an investigator of the Howard Hughes Medical Institute.

351 **Author contributions**

352 D.Y. initiated studies on the ibogaine inward-open conformation. J.A.C. initiated cryo-EM studies  
353 on SERT-antibody complexes. J.A.C, D.Y., and E.G. designed the project. J.A.C and D.Y.  
354 contributed to all aspects of protein purification, biochemical characterization, EM data collection  
355 and processing, and built atomic models. J.A.C. and C.Y. collected the EM data on ts2-inactive  
356 paroxetine and ts2-active ibogaine data sets. J.A.C., C.Y., and D.Y. collected the EM data on  
357  $\Delta$ N72,C13 ibogaine occluded, inward-open, and noribogaine inward-open data sets. J.A.C, D.Y.  
358 and E.G. wrote the manuscript. Z.Z., P.W., and E.T. performed ibogaine docking, MD  
359 simulations, and wrote sections related to computational methods. All authors contributed to  
360 editing and manuscript preparation.

361 **Data Availability Statement**

362 The data that support the findings of this study are available from the corresponding author  
363 upon request. The coordinates for the 15B8 X-ray structure has been deposited in the Protein  
364 Data Bank under the accession code 6D9G. The coordinates and associated volumes for the  
365 cryo-EM reconstruction of ts2-inactive Fab/scFv paroxetine, ts2-active Fab/scFv ibogaine-  
366 outward,  $\Delta$ N72,C13 Fab ibogaine-occluded, and  $\Delta$ N72,C13 Fab ibogaine-inward-open data sets  
367 have been deposited in the Protein Data Bank (PDB) and Electron Microscopy Data Bank  
368 (EMDB) under the accession codes 6DZW and 8941, 6DZY and 8942, 6DZV and 8940, 6DZZ  
369 and 8943 respectively. The volume for the cryo-EM reconstruction of the  $\Delta$ N72,C13 Fab  
370 noribogaine inward-open reconstruction has been deposited in the EMDB under accession code

371 0437. The half-maps and masks used for refinement for each data set have also been  
372 deposited in the EMDB.

373 **Author Information Statement**

374 The authors declare no competing interests. Correspondence and requests for materials should  
375 be addressed to gouauxe@ohsu.edu

376 **FIGURE LEGENDS**

377 **Figure 1. Ibogaine binding, uptake and labeling experiments.** **a**, Ibogaine and serotonin with  
378 the methoxy group and bicyclic cage highlighted by red and green dashed ovals, respectively.  
379 Demethylation of the methoxy group of ibogaine produces noribogaine. **b**, Plots of [<sup>14</sup>C]5-HT  
380 uptake for ts2-active SERT in the absence (blue, squares) or presence (red, open squares) of 1  
381  $\mu$ M 15B8 and 8B6. [<sup>14</sup>C]5-HT uptake for  $\Delta$ N72,C13 SERT (orange, circles) and in the presence  
382 of 1 $\mu$ M 15B8 (green, open circles). Symbols show the mean derived from n=3 biological  
383 replicates. Error bars show the s.e.m. Experiment was performed three times independently  
384 with the same results. **c**, Left panel, plot of a [<sup>3</sup>H]ibogaine saturation binding to ts2-active SERT  
385 (blue, squares) and in the presence of 15B8 (green, circles) in 100 mM NaCl. Symbols show the  
386 mean derived from n=3 technical replicates. Error bars show the s.e.m. Experiment was  
387 performed four times independently with the same results. Right panel, graph of [<sup>3</sup>H]ibogaine  
388 saturation binding to ts2-active SERT in 100 mM KCl (blue, squares), 100 mM NMDG-Cl  
389 (orange, triangles) and in presence of 15B8 in 100 mM KCl (green, circles), symbols show the  
390 mean derived from n=6 biological replicates. Error bars show the s.e.m. Experiment was  
391 performed four times independently with the same results. **d**, Ser277Cys was labeled for 10 min  
392 with 10  $\mu$ M MTS-ACMA in the presence of 100 mM KCl or 100 mM NaCl. The bars show the  
393 means and points show the value for each technical replicate. Error bars show the s.e.m. \*P <  
394 0.05, One-sided student's *t*-test.

395 **Figure 2. Cryo-EM reconstructions of outward-open, occluded and inward-open**  
396 **conformations.** **a**, Outward-open maps of ts2-active SERT (4.1 Å resolution, contour level  
397 ~6.2) bound to 15B8 Fab/8B6 scFv. **b**, Occluded conformation of ΔN72,C13 SERT bound to  
398 15B8 Fab, in 100 mM NaCl (4.2 Å resolution, contour level ~2.7). **c**, Inward-open conformation  
399 of the ΔN72,C13 SERT-15B8 complex, in the presence of 100 mM KCl (3.6 Å resolution,  
400 contour level ~6.7). SERT, 15B8 Fab and 8B6 scFv are in cyan, purple and green respectively;  
401 TM1 is orange and TM6 is red and a CHS molecule is in grey. Movements of TM6a and TM1a  
402 from outward-open (dotted lines) to occluded and inward-open conformations (filled lines) are  
403 indicated.

404 **Figure 3. Ibogaine binding site and conformational changes upon isomerization from the**  
405 **outward-open to the occluded and inward-open states.** Poses of ibogaine (green) from  
406 molecular dynamics studies in the **a**, outward-open, **b**, occluded, and **c**, inward-open  
407 conformations. **d**, Comparison of ibogaine binding poses in outward-open (grey), occluded  
408 (orange) and inward-open (blue) conformations. **e**, The -logIC<sub>50</sub> of each mutant for inhibition of  
409 uptake for ibogaine (blue) or noribogaine (red) is shown. The mean -logIC<sub>50</sub> was determined  
410 using the curves in Extended Data Fig. 8a with the error of the fit (s.e.m.) shown. \*P < 0.05; \*\*P  
411 < 0.01, One-sided student's *t*-test. **f**, [<sup>3</sup>H]-ibogaine saturation binding experiments of Asn177  
412 mutants in 100 mM KCl, and the corresponding mean K<sub>d</sub> values determined using the curves  
413 with the error of fit (s.e.m.): Asn177Val (blue circles, 70 ± 20 nM), Asn177Ala (red squares, 130  
414 ± 40 nM), Asn177Thr (green triangles, 200 ± 20 nM), and Asn177Gln (olive inverted triangles,  
415 140 ± 50 nM); binding of [<sup>3</sup>H]-ibogaine to ts2-active (dotted line) from Figure 1c is shown for  
416 comparison. Symbols show the mean derived from n=6 biological replicates. Error bars show  
417 the s.e.m. Experiment was performed five times independently with the same results. **g**, 'Slab'  
418 views of the extracellular and intracellular cavities in the outward-open (left panel), occluded  
419 (middle panel) and inward-open conformations (right panel). TM1 and TM6 are shown as

420 cartoon representations and are orange and red, respectively. Residues defining the  
421 extracellular and intracellular gate are in sticks. The distance between extracellular (F335 and  
422 Y176) and intracellular gating residues (Y350 and W82) is shown. **h**, Comparison of the  
423 occluded and outward-open (grey) conformations. **i**, Superposition of inward-open and occluded  
424 (grey) conformations.

425 **Figure 4. Mechanisms of transport and ibogaine action.** Cartoon depicts conformational  
426 differences among outward-open, occluded and inward-open conformations. Ibogaine inhibits  
427 SERT either by binding to the outward-open followed by stabilization of the occluded or inward-  
428 open conformations or by directly binding to the inward-open conformation. The scaffold domain  
429 and associated TMs (grey) and TM2, 7, 8, 10, and 12 are shown in light blue. TM1, TM5 and  
430 TM6 are highlighted with orange, red and green. TM 4 and 9 are omitted for clarity. Sodium and  
431 chloride are shown as red and green spheres.

432

433 **METHODS**434 **Data reporting**

435 No statistical methods were used to predetermine sample size. The experiments were not  
436 randomized and the investigators were not blinded to allocation during experiments and  
437 outcome assessment.

438 **Antibody production**

439 The 15B8 Fab was produced either by papain digestion of 15B8 mAb and purified by  
440 cation exchange chromatography, using standard methods<sup>28</sup>, or by isolation from Sf9  
441 supernatant by metal affinity chromatography for crystallization<sup>34</sup>. The 8B6 heavy and light  
442 chains of the variable domain were fused to a PelB signal sequence, an N-terminal 8-His tag,  
443 and connected by a (GGGGS)<sub>3</sub> linker to create the 8B6 scFv. The 8B6 scFv was expressed  
444 overnight at 25°C in BL21 induced with 0.1 mM isopropyl-β-D-1-thiogalactopyranoside.  
445 Periplasmic proteins were extracted by homogenizing cells in 200 mM Tris pH 8, 20% sucrose,  
446 1 mM EDTA, 1 mM phenylmethylsulfonyl fluoride. The buffer was exchanged to 50 mM  
447 phosphate pH 8.0, 300 mM NaCl, 10 mM imidazole by dialysis. The 8B6 scFv was purified by  
448 metal affinity chromatography and size-exclusion chromatography on a Superdex 75 column.

449 **SERT expression and purification**

450 The human SERT constructs used in this study are the N- and C-terminally truncated  
451 wild-type (ΔN72, ΔC13), ts2-active (Ile291Ala, Thr439Ser)<sup>28,35</sup>, C7x made in the ts2-active  
452 background (Cys109Ala, Cys147Ala, Cys155Ser, C166Leu, Cys522Ser, C357Leu, Cys369Leu),  
453 and ts2-inactive (Tyr110Ala, Ile291Ala)<sup>18</sup>. The expression and purification of the aforementioned  
454 constructs was carried out as described previously<sup>28</sup> with minor changes. SERT was expressed  
455 as a C-terminal GFP fusion using baculovirus-mediated transduction of HEK-293S GnTI- cells<sup>36</sup>.  
456 Cells were solubilized in 20 mM Tris pH 8, 150 mM NaCl or 100 mM KCl containing 20 mM n-

457 dodecyl- $\beta$ -D-maltoside (DDM), 2.5 mM cholesteryl hemisuccinate (CHS), in the presence of 1  
458  $\mu$ M paroxetine, or 10  $\mu$ M ibogaine, or 10  $\mu$ M noribogaine and purified into 1 mM DDM, 0.2 mM  
459 CHS, and 1  $\mu$ M paroxetine, or 10  $\mu$ M ibogaine, or 10  $\mu$ M noribogaine in 20 mM Tris pH 8, 100  
460 mM NaCl or 100 mM KCl by Strep-Tactin affinity. The N- and C-terminal GFP and purification  
461 tags were removed by thrombin digestion. For the SERT-Fab/scFv complex, 15B8 Fab and 8B6  
462 ScFv were mixed with SERT at a 1:1.2:1.2 molar ratio and purified by size-exclusion on a  
463 Superdex 200 column in TBS (20 mM Tris pH 8, 100 mM NaCl) containing 9 mM  
464 nonylmaltoside, 0.2 mM CHS, 1  $\mu$ m paroxetine or 10  $\mu$ M ibogaine. For the  $\Delta$ N72,C13 SERT-  
465 Fab complex, 15B8 Fab was mixed with SERT at a 1:1.2 ratio and separated by size-exclusion  
466 on a Superdex 200 column in 20 mM Tris pH 8, 100 mM NaCl or 100 mM KCl containing 1 mM  
467 DDM, 0.2 mM CHS, 10  $\mu$ M ibogaine or 10  $\mu$ M noribogaine. The peak fraction containing the  
468 SERT complexes was concentrated to 4 mg/ml prior to adding either 250  $\mu$ M paroxetine, 1 mM  
469 ibogaine or 1 mM noribogaine.

470 **Crystallization of 15B8 Fab**

471 The 15B8 Fab was crystallized by hanging drop vapor diffusion (Extended Data Table 2).  
472 Crystals appeared after several days under conditions with a reservoir solution composed of 80  
473 mM sodium citrate pH 5.2, 2.2 M ammonium sulfate at a 1:1 ratio of protein:reservoir. The 15B8  
474 Fab crystals were cryoprotected with 25% ethylene glycol prior to flash cooling in liquid nitrogen.

475 **Cryo-EM sample preparation and data acquisition**

476 The SERT-antibody complexes (2.5  $\mu$ l) at a concentration of 40-80  $\mu$ M were applied to  
477 glow-discharged Quantifoil holey carbon grids (gold, 1.2/1.3 or 2.0/2.0  $\mu$ m size/hole space, 200  
478 mesh). For ‘multi-shot’ data collection<sup>37</sup>, 100  $\mu$ M fluorinated n-octyl- $\beta$ -D-maltoside (final  
479 concentration) was added to the sample prior to freezing. The grids were blotted for 1.5-2.5 s at  
480 100% humidity using a Vitrobot Mark IV, followed by plunging into liquid ethane cooled by liquid

481 nitrogen. Images were acquired using a FEI Titan Krios equipped with a Gatan Image Filter  
482 operating at 300 kV or an Arctica transmission electron microscope (TEM) at 200 kV. A Gatan  
483 K2 Summit direct electron detector was used, on both TEMs, to record movies in super-  
484 resolution counting mode with a binned pixel size of 1.044 or 0.823 Å/pixel on the Krios or 0.910  
485 Å/pixel on the Arctica, respectively. The defocus values ranged from -1.0 to -2.5 μm. Exposures  
486 of 8-10 s were dose-fractionated into 40-100 frames, resulting in a total dose of 50-60 e<sup>-</sup>/Å<sup>2</sup>.  
487 Images were recorded using the automated acquisition program SerialEM<sup>37</sup>.

488 **Image processing**

489 Micrographs were corrected for beam-induced drift using MotionCor2<sup>38</sup>. The contrast  
490 transfer function (CTF) parameters for each micrograph were determined using GCTF<sup>39</sup>.  
491 Particles were picked using DoG-picker<sup>40</sup>. Particles were subjected to reference-free 2D  
492 classification in either RELION 2.1<sup>41</sup> or CryoSPARC<sup>42</sup> followed by homogenous refinement in  
493 CryoSPARC. Local refinement was performed in cisTEM<sup>43</sup> with a mask which excludes the  
494 micelle and Fab constant domain to remove low resolution features (Extended Data Fig. 2-5).  
495 The molar masses of the SERT-15B8 Fab/8B6 scFv and SERT-15B8 Fab complexes were 135  
496 and 105 kDa respectively. Focused 3D classification<sup>44</sup> was also performed in cisTEM using a  
497 spherical mask centered on SERT to discover additional conformational heterogeneity. The  
498 resolution of the reconstructions was assessed using the FSC criterion and a threshold of  
499 0.143<sup>45</sup> in cisTEM<sup>43</sup>. The low-resolution refinement limit was incrementally increased while  
500 maintaining a correlation of 0.95 or greater until no further improvement in map quality was  
501 observed. The FSC of the model vs. the full map and half-maps were calculated using the  
502 standalone program calculate\_fsc which is part of the cisTEM package. The local resolution was  
503 calculated using RELION 3.0. Maps were sharpened using cisTEM unless otherwise noted.

504 For the ts2-inactive paroxetine Fab/scFv data set, a total of 1,278,876 particles with a  
505 box size of 240 pixels were selected from 2,904 micrographs (Extended Data Fig. 2a). After two

506 rounds of 2D classification using CryoSPARC, particles that had clearly defined and  
507 recognizable features were combined for further analysis. CryoSPARC was used to generate an  
508 *ab-initio* model with 2 classes. Particles belonging to a class with well-defined features were  
509 further refined using local refinement in cisTEM. The low-resolution limit cutoff for refinement  
510 was 7.5 Å. The map was sharpened using local sharpening in Phenix<sup>46</sup>. For the ts2-active  
511 ibogaine Fab/scFv data set, a total of 592,117 particles with a box size of 300 pixels were  
512 selected from 1,639 micrographs. After rounds of 2D classification and *ab-initio* reconstruction  
513 using CryoSPARC, 153,986 particles that had clearly defined features were selected. Particle  
514 coordinates were used to calculate the local CTF using GCTF and local refinement was  
515 performed in cisTEM (Extended Data Fig. 3a). The low-resolution limit cutoff for refinement was  
516 7.5 Å. The optimal sharpening *B* factor of -400 Å<sup>2</sup> inside the same mask used for refinement  
517 was determined by comparing map features for various sharpening factors in cisTEM. A similar  
518 strategy was used for ΔN72,C13-15B8 Fab complex with ibogaine in NaCl. A total 2,615,403  
519 particles with a box size of 360 pixels were selected from 10,632 micrographs followed by  
520 rounds of 2D classification, *ab-initio* reconstruction and homogeneous refinement using  
521 CryoSPARC. The final particle set contained 724,394 particles which were subjected for local  
522 refinement using cisTEM (Extended Data Fig. 4a). The low-resolution limit cutoff for refinement  
523 was 7.0 Å. For the ΔN72,C13-15B8 Fab complex with ibogaine in 100 mM KCl containing buffer,  
524 1,220,861 particles with a box size of 380 pixels were selected from 7,732 micrographs. After  
525 multiple rounds of 2D classification, *ab-initio* reconstruction, 3D classification in RELION 2.1,  
526 and homogeneous refinement using cryoSPARC, 383,617 particles were subjected to local  
527 refinement in cisTEM. (Extended Data Fig. 5a). The low-resolution limit cutoff for refinement was  
528 7.5 Å.

529 **Model building and refinement**

530 Interpretation of the cryo-EM maps relied upon rigid body fitting of the higher resolution  
531 SERT and antibody models derived from x-ray crystallography. While the quality of the EM  
532 maps precludes a precise analysis of atom-atom interactions, we were able to model the main  
533 chain of SERT and position most bulky side-chains. A starting model was generated by fitting  
534 SERT (PDB code: 6AWN)<sup>18</sup> into the outward-open ibogaine bound reconstruction together with  
535 the variable domains of 8B6 (PDB code: 5I66) and 15B8 (PDB code: 6D9G, Extended Data  
536 Table 2) Fabs derived from high-resolution crystal structures in Chimera<sup>47</sup>. Model refinement  
537 was performed in Rosetta using iterative local rebuilding<sup>48</sup>. Models were scored according to the  
538 fit to the density and overall Rosetta score. The best models were selected and used as  
539 templates for further refinement in RosettaCM. The paroxetine-bound model was refined  
540 separately in RosettaCM starting from SERT (PDB code: 6AWN) with the variable domains of  
541 8B6 and 15B8. To build the occluded and inward-open conformation models, the 8B6 variable  
542 domain was removed from the outward-open ibogaine ts2-active model followed by fitting of the  
543 model into the occluded or inward-open reconstructions. Several rounds of iterative local  
544 rebuilding were performed, followed by combining pieces from multiple templates and  
545 refinement with RosettaCM. The final stages of model building involved manual adjustments  
546 and building where merited by the quality of the EM maps in Coot<sup>49</sup> followed by real space  
547 refinement in Phenix. For cross-validation, the FSC curve between the refined model and half-  
548 maps was calculated and compared to avoid overfitting. Molprobity was used to evaluate the  
549 stereochemistry and geometry of the structures<sup>50</sup>. For the outward-open and occluded  
550 reconstructions, residues 79-615 were modeled into the cryo-EM maps while residues 78-617  
551 were modeled for the inward-open reconstruction. This strategy, coupled with docking and  
552 molecular dynamics (MD) simulations, furthered our interpretation of the large-scale  
553 rearrangements of structural elements in each conformation and provided a basis for molecular  
554 details of ibogaine interactions within the central site. Figures were prepared in PyMOL<sup>51</sup> and

555 Chimera<sup>47</sup>. The profile of the intracellular pathways shown in ED Figure 10b,c was calculated  
556 using Caver<sup>52</sup>.

557 **Measurements**

558 All distance measurements represent the center of mass calculated from C $\alpha$  positions.  
559 Extracellular measurements were made from Tyr186 in TM3 to marker positions in TM1b  
560 (Gln111), 2 (Ala116), 4 (Gln254), 5 (Gly299), 6a (Asp328), 7 (Met386), 8 (Thr421), 9 (Thr480),  
561 10 (Ala486), 11 (Phe556), and 12 (Ser574). Intracellular measurements were made from Gly160  
562 in TM3 to marker positions in TM1a (Lys85), 2 (His143), 4 (Tyr267), 5 (Trp282), 6b (Ser349), 7  
563 (Tyr358), 8 (Glu453), 9 (Arg462), 10 (Phe515), 11 (Trp535), and 12 (Ile599). To measure the  
564 angular change between conformations, the TM helices were superimposed and the angle  
565 between helices was measured using C $\alpha$  positions in PyMOL. The uncertainty of each  
566 measurement and the position of ibogaine was calculated from 100 models which were  
567 randomly perturbing by ~1.0 Å RMSD and real space refined back into each map in Phenix, as  
568 described<sup>53</sup>. The solvent accessible surface area of the allosteric site was calculated from  
569 residues within 5 Å of S-citalopram structure (PDB code: 5i73); residues (100, 103-105, 175,  
570 327-338, 368, 490-503, 549-557, 561, 563, 579).

571 **Protein preparation for docking and molecular dynamics simulations**

572 The outward-open ts2-active, occluded  $\Delta$ N72,C13, and inward-open  $\Delta$ N72,C13  
573 conformations of SERT were prepared for simulations by removing antibodies, adding missing  
574 hydrogen atoms and side chains in PSFGEN<sup>54</sup>, and by removing CHS from the occluded  
575 conformation. For the outward-open conformation, the backbones of Gly83, Lys84, Thr219, and  
576 Trp220 were corrected to a trans form using the CISPEPTIDE plugin<sup>55</sup> of VMD<sup>54</sup>. Glu136 and  
577 Glu508 were modeled with protonated side chains according to pKa calculations using PROPKA  
578 3.0<sup>56</sup> for the outward-open and inward-open conformations. For the outward-open and occluded  
579 conformations, two Na<sup>+</sup> and one Cl<sup>-</sup> ion were modeled based on the (S)-citalopram and

580 paroxetine-bound x-ray structures of SERT (PDB codes: 5I71 and 5I6X)<sup>28</sup>, while a Cl<sup>-</sup> ion was  
581 modeled in the inward-open conformation. The models were aligned with the orientation of the  
582 paroxetine-bound SERT crystal structure (5I6X) from the OPM (Orientation of Protein in  
583 Membranes) database<sup>57</sup>, available at: [<http://opm.phar.umich.edu/>].

584 **Force field parameterization**

585 The force field parameters of protonated ibogaine were developed based on the  
586 CHARMM General Force Field (CGenFF)<sup>58</sup>. The atom types and initial parameters were  
587 determined using the CGenFF webserver [<https://cgenff.paramchem.org>]<sup>58,59</sup>, and the  
588 parameters were further optimized using the Force Field Toolkit (ffTK)<sup>60</sup> plugin of VMD. The  
589 detailed strategy of optimizing parameters are described as follows. First, partial atomic charges  
590 were assigned to aliphatic carbon and hydrogen atoms according to the convention of  
591 CHARMM force fields (+0.09e per aliphatic hydrogen, neutralized by the negative charge  
592 assigned to the carbon atom carrying hydrogens). The partial atomic charges of the  
593 methoxyindole group were optimized according to the calculated water interactions of the  
594 corresponding atoms in the model compound (5-methoxy-2,3-dimethylindole, MDI) at the HF/6-  
595 31G\* level. The partial charges of the tertiary amine group were assigned as protons at +0.32e  
596 and nitrogen at -0.40e, and all three  $\alpha$ -carbons were assigned equal partial charges at +0.21e  
597 so that a sum of +1e net charge at the tertiary amine group was satisfied. This partial charge  
598 assignment scheme is based on those of other tertiary amine species in CGenFF (e.g., *N*-  
599 methylpiperidine).

600 The bonded parameters of ibogaine also contain 2 novel bonds, 11 novel angles, and 41  
601 novel dihedrals that were not defined in the standard CGenFF force field. All of these  
602 parameters except two dihedrals were directly adopted from the initial parameter set generated  
603 from the CGenFF webserver through analogy to existing parameters without further  
604 optimization, a standard procedure for CGenFF parameters with low predicted penalty

605 scores<sup>59,61</sup> (assigned by the CGenFF webserver). The only two dihedral terms which were  
606 optimized were both centered around the rotation of the bond connecting positions 2 and 3 of  
607 the indole ring, which were calibrated with a 180° dihedral scan at 15° intervals using the  
608 MP2/6-31G\* level of theory on the MDI model compound. All quantum mechanical calculations  
609 were performed using Gaussian09<sup>62</sup> [<http://gaussian.com/glossary/g09/>].

610 **Computational search for docking poses of ibogaine**

611 A workflow (Extended Data Fig. 7a, Supplementary Video 2) was developed to  
612 systematically search for optimal binding poses of ibogaine in the outward-open, occluded, and  
613 inward-open conformations of SERT, independently. Using the approximate geometric center of  
614 the binding pocket (defined as Tyr95, Ala96, Asp98, Ile172, Ala173, Tyr175, Phe335, Ser336,  
615 Gly338, Phe341, Ser438, Gly442, Leu443, Thr497, Gly498, and Val501) as the origin, a 6 × 6 ×  
616 6 search grid (1- Å spacing) was defined. For each conformation of SERT, an energy-minimized  
617 copy of ibogaine was placed at every grid point, rotated around all combinations of three Euler  
618 angles (at 18° intervals), and all six rotameric forms of the methoxy and ethyl groups which  
619 resulted in 7.5 million SERT-ibogaine models with different ibogaine poses. These poses were  
620 analyzed using the following four steps: 1) a 20-step energy minimization of all the SERT-  
621 ibogaine models in NAMD2<sup>63</sup> to remove straightforward steric clashes, during which the protein  
622 backbone was not allowed to move; 2) calculating pair interaction energy (PIE) between  
623 ibogaine and the protein by evaluating the sum of van der Waals and electrostatic interaction  
624 energies with the PAIRINTERACTION module in NAMD2<sup>63</sup>, only ibogaine poses with negative  
625 (favorable) PIE are included in the clustering step; 3) clustering of binding poses of ibogaine  
626 based on the mass-weighted root-mean-square deviation (RMSD) of ibogaine using a hybrid k-  
627 centers k-medoids clustering method<sup>64</sup> with a 2-Å cutoff; and 4) disposing insignificant clusters  
628 of binding poses, defined as those with <1% population, or those with negative ΔCCC (the  
629 difference in the cross-correlation coefficient with the cryo-EM density between the model with

630 and the model without ibogaine). Steps 1-4 were iterated until the number of clusters  
631 converged. From the resulting final clusters (20 clusters for outward-open, 30 for occluded, and  
632 46 for inward-open), the SERT-ibogaine model with the strongest PIE in each cluster was  
633 selected for an additional 3000 steps of minimization and a 10-ns MD simulation in NAMD2<sup>63</sup>  
634 (96 independent simulations in total) in a membrane environment (see Methods describing  
635 'Molecular dynamics simulations'). During these steps the protein backbone atoms were  
636 harmonically restrained with a 1 kcal/mol/Å<sup>2</sup> force constant. Simulation trajectories were  
637 recorded every 10 ps. The first 2 ns were discarded to allow for equilibration, resulting in 800  
638 snapshots of ibogaine per simulation. For each SERT conformation, the resulting snapshot sets  
639 (20 for outward-open, 30 for occluded, and 46 for inward-open, each set with 800 snapshots)  
640 were ranked by their averaged ΔCCC, from which the best snapshot set was selected for each  
641 SERT conformation. From these highest-ranked sets the ibogaine pose with the highest ΔCCC  
642 was selected as the optimal pose for each conformation.

#### 643 **Molecular dynamics (MD) simulations**

644 The following procedures were used for all the MD simulations performed on ligand-  
645 bound SERT systems. Each SERT-ibogaine model was first internally hydrated by adding water  
646 molecules with the Dowser plugin<sup>65</sup> of VMD, followed by the insertion of the hydrated protein  
647 into a lipid bilayer composed of 236 1-palmitoyl-2-oleoyl-sn-glycero-3-phosphocholine (POPC)  
648 molecules obtained from CHARMM-GUI<sup>66</sup>, and solvated with ~100 mM of NaCl (for outward-  
649 open and occluded) or ~100 mM of KCl (for inward-open) in VMD<sup>54</sup>, resulting in a box of  
650 ~100×100×105 Å<sup>3</sup> dimensions containing ~100,000 atoms.

651 To investigate the stability of the ibogaine binding poses determined by the ligand  
652 docking procedure, two 50-ns simulations were performed with each ibogaine-bound  
653 conformation (3 systems in total) in a POPC lipid bilayer, resulting in six trajectories. After 3,000  
654 steps of minimization, the systems were equilibrated for 600 ps, during which Cα atoms, non-

655 hydrogen atoms of ibogaine and the bound ions were restrained by harmonic potentials with  
656 decreasing force constants ( $k=1$ , 0.5, and 0.1 kcal/mol/Å<sup>2</sup> for 200 ps each) to allow for relaxation  
657 of protein side chains and hydration of the protein. Weak harmonic potentials ( $k = 0.1$   
658 kcal/mol/Å<sup>2</sup>) were applied to the C $\alpha$  atoms (excluding N- and C-termini).

659 The same simulation protocols were applied to both 10-ns and 50-ns MD simulations. All  
660 simulations were performed using NAMD2<sup>63</sup> and CHARMM36m force fields<sup>67</sup> for SERT,  
661 CHARMM36 force fields<sup>68</sup> for lipids, and the TIP3P model<sup>69</sup> for water. The force field parameters  
662 for ibogaine were developed based on the CGenFF<sup>58</sup>, with further optimization using ffTK (see  
663 Force field parameterization)<sup>60</sup>. All simulations were carried out as NPT ensembles, where the  
664 system pressure was independently coupled along the XY (membrane plane) and Z (membrane  
665 normal) dimensions to allow for their independent changes. Constant temperature was  
666 maintained at 310 K using Langevin dynamics with a 1.0 ps<sup>-1</sup> damping coefficient, while  
667 constant pressure was maintained at 1.01325 bar with the Langevin piston Nosé-Hoover  
668 method<sup>70,71</sup>. Non-bonded interactions were calculated in a pairwise manner within the 12 Å  
669 cutoff, with a switching function applied between 10-12 Å. Long-range non-bonded interactions  
670 were calculated with the particle mesh Ewald (PME) method<sup>72</sup>. Bond lengths involving hydrogen  
671 atoms were fixed using the SHAKE algorithm<sup>73</sup>. Simulations were integrated in 2-fs time steps,  
672 and trajectories recorded every 10 ps.

673 **Data analysis of simulation trajectories**

674 Hybrid k-centers k-medoids clustering<sup>64</sup> was done with MDToolbox  
675 [<https://mdtoolbox.readthedocs.io/en/latest/introduction.html>]. Trajectory analysis was carried out  
676 in VMD<sup>54</sup> and MDAnalysis<sup>74,75</sup>. VMD was used for visualization. The cross-correlation coefficient  
677 between the cryo-EM map and the model was calculated using the Molecular Dynamics Flexible  
678 Fitting plugin<sup>76</sup>. PIE was calculated in NAMD2<sup>63</sup>. The RMSD and distance plots were smoothed  
679 using a sliding window of 50 frames (0.5 ns).

680 **Reconstitution and labeling of SERT in nanodiscs**

681 The Ser277Cys mutant was introduced into the C7x variant in which all reactive  
682 endogenous cysteines have been mutated. For labeling studies, purified SERT was mixed with  
683 soybean asolectin and MSP1E3D1<sup>77</sup> and reconstituted into nanodiscs at a molar ratio of 1:5:400  
684 to reduce background labeling. Detergent was removed by incubation with biobeads overnight  
685 at room temperature, followed by size-exclusion chromatography on a Superdex 200 column in  
686 TBS. SERT in nanodiscs was incubated with 1 mM ibogaine or 0.2 mM paroxetine for 30  
687 minutes at room temperature, followed by labeling with 10  $\mu$ M MTS-ACMA for the indicated  
688 time. Labeled SERT was desalted and analyzed on a non-reducing SDS-PAGE gel.

689 **Radioligand binding and uptake assays**

690 To measure uptake,  $1 \times 10^5$  HEK-293S GnT $\alpha$ - cells transduced with either ts2-active,  
691 Asn177 mutants or  $\Delta$ N72,C13 SERT were plated into 96-well plates coated with poly-D-lysine.  
692 After 24 hrs, cells were washed with uptake buffer (25 mM HEPES-Tris, pH 7.0, 130 mM NaCl,  
693 5.4 mM KCl, 1.2 mM CaCl<sub>2</sub>, 1.2 mM MgSO<sub>4</sub>, 1 mM ascorbic acid and 5 mM glucose). In some  
694 cases, antibodies were added to cells at a concentration of 1  $\mu$ M which is in excess of the  
695 estimated  $K_D$  for the 8B6 scFv and the 15B8 Fab (< 10 nM). To measure the background  
696 counts, 100  $\mu$ M paroxetine was added to the cells. [<sup>3</sup>H]5-hydroxytryptamine (5-HT) diluted 1:500  
697 with unlabeled 5-HT, or [<sup>14</sup>C]5-HT at concentrations of 0.03–40.0  $\mu$ M was also added to the  
698 cells. In the case of [<sup>3</sup>H]5-HT, uptake was stopped by rapidly washing cells 3x with 100  $\mu$ l uptake  
699 buffer, solubilizing with 20  $\mu$ l of 1% Triton-X100, followed by addition of 200  $\mu$ l of scintillation  
700 fluid to each well. The amount of labeled 5-HT was measured by counting in a standard 96-well  
701 plate or in a Cytostar-T plate using a MicroBeta scintillation counter. Data were fit to a  
702 Michaelis–Menten equation.

703 Competition binding experiments were performed using scintillation proximity assays  
704 (SPA) with 5 nM SERT, 0.5 mg/ml Cu-Ysi beads in TBS containing 1 mM DDM, 0.2 mM CHS,  
705 and 5 nM [<sup>3</sup>H]paroxetine and at 0.1nM–1 mM of the cold competitors. Where indicated,  
706 antibodies were added to SERT at a concentration of 1  $\mu$ M. Experiments were measured in  
707 triplicate, and each experiment was performed three times. The error bars for each data point  
708 represent the s.e.m.  $K_i$  values were determined with the Cheng–Prusoff equation<sup>78</sup> in GraphPad  
709 Prism.

710 Ibogaine binding was measured via SPA using ts2-active SERT purified in SPA buffer (20  
711 mM Tris pH 8, 100 mM NaCl or 100 mM KCl containing 50  $\mu$ M lauryl maltose neopentyl glycol  
712 and 10  $\mu$ M CHS). Each experiment contained SERT at a concentration of 50 nM mixed with 0.5  
713 mg/ml Cu Ysi beads and [<sup>3</sup>H]ibogaine at a concentration of 15-4000 nM (1:10 hot:cold) in SPA  
714 buffer. The background was determined by addition of 100  $\mu$ M paroxetine to SERT. In the case  
715 of binding experiments in KCl or NMDG the buffer was also supplemented with 25 mM NaCl to  
716 measure the background. Data was analyzed as a single-site binding function.

## 717 ONLINE ONLY REFERENCES

718 34 Coleman, J. A., Green, E. M. & Gouaux, E. Thermostabilization, expression, purification,  
719 and crystallization of the human serotonin transporter bound to s-citalopram. *J Vis Exp*,  
720 (2016).

721 35 Green, E. M., Coleman, J. A. & Gouaux, E. Thermostabilization of the human serotonin  
722 transporter in an antidepressant-bound conformation. *PLoS One* **10**, e0145688, (2015).

723 36 Goehring, A. *et al.* Screening and large-scale expression of membrane proteins in  
724 mammalian cells for structural studies. *Nat Protoc* **9**, 2574-2585, (2014).

725 37 Mastronarde, D. N. Automated electron microscope tomography using robust prediction  
726 of specimen movements. *J Struct Biol* **152**, 36-51, (2005).

727 38 Zheng, S. Q. *et al.* MotionCor2: anisotropic correction of beam-induced motion for  
728 improved cryo-electron microscopy. *Nat Methods* **14**, 331-332, (2017).

729 39 Zhang, K. Gctf: Real-time CTF determination and correction. *J Struct Biol* **193**, 1-12,  
730 (2016).

731 40 Voss, N. R., Yoshioka, C. K., Radermacher, M., Potter, C. S. & Carragher, B. DoG Picker  
732 and TiltPicker: software tools to facilitate particle selection in single particle electron  
733 microscopy. *J Struct Biol* **166**, 205-213, (2009).

734 41 Scheres, S. H. RELION: implementation of a Bayesian approach to cryo-EM structure  
735 determination. *J Struct Biol* **180**, 519-530, (2012).

736 42 Punjani, A., Rubinstein, J. L., Fleet, D. J. & Brubaker, M. A. cryoSPARC: algorithms for  
737 rapid unsupervised cryo-EM structure determination. *Nat Methods* **14**, 290-296, (2017).

738 43 Grant, T., Rohou, A. & Grigorieff, N. cisTEM, user-friendly software for single-particle  
739 image processing. *Elife* **7**, (2018).

740 44 Zhang, C. *et al.* Analysis of discrete local variability and structural covariance in  
741 macromolecular assemblies using Cryo-EM and focused classification. *Ultramicroscopy*,  
742 (2018).

743 45 Rosenthal, P. B. & Henderson, R. Optimal determination of particle orientation, absolute  
744 hand, and contrast loss in single-particle electron cryomicroscopy. *J Mol Biol* **333**, 721-  
745 745, (2003).

746 46 Adams, P. D. *et al.* PHENIX: a comprehensive Python-based system for macromolecular  
747 structure solution. *Acta Crystallogr D Biol Crystallogr* **66**, 213-221, (2010).

748 47 Pettersen, E. F. *et al.* UCSF Chimera--a visualization system for exploratory research  
749 and analysis. *J Comput Chem* **25**, 1605-1612, (2004).

750 48 Wang, R. Y. *et al.* Automated structure refinement of macromolecular assemblies from  
751 cryo-EM maps using Rosetta. *Elife* **5**, (2016).

752 49 Emsley, P. & Cowtan, K. Coot: model-building tools for molecular graphics. *Acta  
753 Crystallogr D Biol Crystallogr* **60**, 2126-2132, (2004).

754 50 Chen, V. B. *et al.* MolProbity: all-atom structure validation for macromolecular  
755 crystallography. *Acta Crystallogr D Biol Crystallogr* **66**, 12-21, (2010).

756 51 The PyMOL molecular graphics system, Version 2.0 Schrödinger, LLC.

757 52 Chovancova, E. *et al.* CAVER 3.0: a tool for the analysis of transport pathways in  
758 dynamic protein structures. *PLoS Comput Biol* **8**, e1002708, (2012).

759 53 Afonine, P. V. *et al.* New tools for the analysis and validation of cryo-EM maps and  
760 atomic models. *Acta Crystallogr D Struct Biol* **74**, 814-840, (2018).

761 54 Humphrey, W., Dalke, A. & Schulten, K. VMD: visual molecular dynamics. *J Mol Graph*  
762 **14**, 33-38, 27-38, (1996).

763 55 Schreiner, E., Trabuco, L. G., Freddolino, P. L. & Schulten, K. Stereochemical errors and  
764 their implications for molecular dynamics simulations. *BMC Bioinformatics* **12**, 190,  
765 (2011).

766 56 Olsson, M. H., Sondergaard, C. R., Rostkowski, M. & Jensen, J. H. PROPKA3:  
767 consistent treatment of internal and surface residues in empirical pKa predictions. *J  
768 Chem Theory Comput* **7**, 525-537, (2011).

769 57 Lomize, M. A., Pogozheva, I. D., Joo, H., Mosberg, H. I. & Lomize, A. L. OPM database  
770 and PPM web server: resources for positioning of proteins in membranes. *Nucleic Acids  
771 Res* **40**, D370-376, (2012).

772 58 Vanommeslaeghe, K. *et al.* CHARMM general force field: A force field for drug-like  
773 molecules compatible with the CHARMM all-atom additive biological force fields. *J  
774 Comput Chem* **31**, 671-690, (2010).

775 59 Vanommeslaeghe, K., Raman, E. P. & MacKerell, A. D., Jr. Automation of the CHARMM  
776 General Force Field (CGenFF) II: assignment of bonded parameters and partial atomic  
777 charges. *J Chem Inf Model* **52**, 3155-3168, (2012).

778 60 Mayne, C. G., Saam, J., Schulten, K., Tajkhorshid, E. & Gumbart, J. C. Rapid  
779 parameterization of small molecules using the Force Field Toolkit. *J Comput Chem* **34**,  
780 2757-2770, (2013).

781 61 Vanommeslaeghe, K. & MacKerell, A. D., Jr. Automation of the CHARMM General Force  
782 Field (CGenFF) I: bond perception and atom typing. *J Chem Inf Model* **52**, 3144-3154,  
783 (2012).

784 62 Gaussian 09, Revision A.02 (Gaussian, Inc., 2016).

785 63 Phillips, J. C. *et al.* Scalable molecular dynamics with NAMD. *J Comput Chem* **26**, 1781-  
786 1802, (2005).

787 64 Beauchamp, K. A. *et al.* MSMBuilder2: modeling conformational dynamics at the  
788 picosecond to millisecond scale. *J Chem Theory Comput* **7**, 3412-3419, (2011).  
789 65 Gumbart, J., Trabuco, L. G., Schreiner, E., Villa, E. & Schulten, K. Regulation of the  
790 protein-conducting channel by a bound ribosome. *Structure* **17**, 1453-1464, (2009).  
791 66 Jo, S., Kim, T., Iyer, V. G. & Im, W. CHARMM-GUI: a web-based graphical user interface  
792 for CHARMM. *J Comput Chem* **29**, 1859-1865, (2008).  
793 67 Huang, J. *et al.* CHARMM36m: an improved force field for folded and intrinsically  
794 disordered proteins. *Nat Methods* **14**, 71-73, (2017).  
795 68 Klauda, J. B. *et al.* Update of the CHARMM all-atom additive force field for lipids:  
796 validation on six lipid types. *J Phys Chem B* **114**, 7830-7843, (2010).  
797 69 Jorgensen, W. L., Chandrasekhar, J., Madura, J. D., Impey, R. W. & Klein, M. L.  
798 Comparison of simple potential functions for simulating liquid water. **79**, 926-935,  
799 (1983).  
800 70 Feller, S. E., Zhang, Y., Pastor, R. W. & Brooks, B. R. Constant pressure molecular  
801 dynamics simulation: The Langevin piston method. **103**, 4613-4621, (1995).  
802 71 Martyna, G. J., Tobias, D. J. & Klein, M. L. Constant pressure molecular dynamics  
803 algorithms. **101**, 4177-4189, (1994).  
804 72 Darden, T., York, D. & Pedersen, L. Particle mesh Ewald: An N·log(N) method for Ewald  
805 sums in large systems. **98**, 10089-10092, (1993).  
806 73 Ryckaert, J.-P., Ciccotti, G. & Berendsen, H. J. C. Numerical integration of the cartesian  
807 equations of motion of a system with constraints: molecular dynamics of n-alkanes.  
808 *Journal of Computational Physics* **23**, 327-341, (1977).  
809 74 Gowers, R. *et al.* MDAnalysis: a python package for the rapid analysis of molecular  
810 dynamics simulations. (2016).  
811 75 Michaud-Agrawal, N., Denning, E. J., Woolf, T. B. & Beckstein, O. MDAnalysis: a toolkit  
812 for the analysis of molecular dynamics simulations. *J Comput Chem* **32**, 2319-2327,  
813 (2011).  
814 76 Trabuco, L. G., Villa, E., Mitra, K., Frank, J. & Schulten, K. Flexible fitting of atomic  
815 structures into electron microscopy maps using molecular dynamics. *Structure* **16**, 673-  
816 683, (2008).  
817 77 Bayburt, T. H. & Sligar, S. G. Membrane protein assembly into nanodiscs. *FEBS Lett*  
818 **584**, 1721-1727, (2010).  
819 78 Cheng, Y. & Prusoff, W. H. Relationship between the inhibition constant (K1) and the  
820 concentration of inhibitor which causes 50 per cent inhibition (I50) of an enzymatic  
821 reaction. *Biochem Pharmacol* **22**, 3099-3108, (1973).  
822 79 Singh, S. K., Piscitelli, C. L., Yamashita, A. & Gouaux, E. A competitive inhibitor traps  
823 LeuT in an open-to-out conformation. *Science* **322**, 1655-1661, (2008).  
824  
825

826 **EXTENDED DATA TABLES**827 **Extended Data Table 1. Cryo-EM data collection, refinement and validation statistics\***

828 \*Data set #1 is the ts2-inactive paroxetine 15B8 Fab/8B6 scFv reconstruction, #2 is the ts2-  
829 active ibogaine outward-open 15B8 Fab/8B6 scFv, #3  $\Delta$ N72,C13 ibogaine occluded 15B8 Fab,  
830 #4  $\Delta$ N72,C13 ibogaine inward-open 15B8 Fab, #5  $\Delta$ N72,C13 noribogaine inward-open 15B8  
831 Fab.

832 <sup>†</sup>Local resolution range.

833 <sup>‡</sup>Resolution at which FSC between map and model is 0.5.

834 **Extended Data Table 2. Data collection and refinement (statistics for x-ray structure of  
835 15B8 Fab)**

836 \*A single crystal was used to determine the 15B8 Fab structure.

837 <sup>†</sup>Values in parentheses are for highest-resolution shell.

838 **EXTENDED DATA FIGURE LEGENDS**

839 **Extended Data Figure 1. Non-competitive inhibition of transport by ibogaine, ibogaine  
840 binding to outward-open, detection of the inward-open conformation, and the paroxetine  
841 ts2-inactive reconstruction. a,** Ibogaine inhibition of 5-HT transport for wild type (blue, circles)  
842 and ts2 (red, squares) variants using 20  $\mu$ M [ $^3$ H]5-HT. Symbols show the mean derived from  
843 n=3 biological replicates. Error bars show the s.e.m. Experiment was performed three times  
844 independently with the same results. **b,** Michaelis–Menten plots of 5-HT uptake for wild type  
845 (blue) transporter in the absence (circles), or in the presence (dash, circles) of 5  $\mu$ M ibogaine,  
846 and for ts2 (red) in the absence (squares), or in the presence (dash, squares) of 5  $\mu$ M ibogaine.  
847 Symbols show the mean derived from n=3 biological replicates. Error bars show the s.e.m.  
848 Experiment was performed three times independently with the same results. The mean  $K_m$  and

849 error (s.e.m.) of curve fitting for  $\Delta$ N72,C13:  $2.2 \pm 0.3 \mu\text{M}$ ; ts2-active:  $4 \pm 1 \mu\text{M}$ . **c**, Competition  
850 binding of ibogaine with [ $^3\text{H}$ ]paroxetine for ts2 in the absence (filled squares) or presence (open  
851 squares) of  $1\mu\text{M}$  15B8 and 8B6 yields a  $K_i$  value  $3.2 \pm 0.4 \mu\text{M}$ . Symbols show the mean derived  
852 from n=3 technical replicates. Error bars show the s.e.m. The mean  $K_i$  and error (s.e.m.) of  
853 curve fitting are reported. Experiment was performed three times independently with the same  
854 results. **d**, [ $^3\text{H}$ ]-ibogaine saturation binding experiments of ts2-inactive and ts2-active 15B8  
855 Fab/8B6 scFv complex in 100 mM NaCl, and corresponding mean  $K_d$  values derived from the  
856 curve fit: ts2-inactive (filled squares,  $> 5 \mu\text{M}$ ), ts2-active 15B8 Fab/8B6 scFv complex (open  
857 triangles,  $> 8 \mu\text{M}$ ). Symbols show the mean derived from n=6 biological replicates. Error bars  
858 show the s.e.m. Experiment was performed twice with similar results. **e**, SDS-PAGE of  
859 Ser277Cys labeling with MTS-ACMA compared with the C7X construct in nanodiscs in the  
860 presence of 1 mM ibogaine and 100 mM NaCl. There is no detectable labeling of the C7X  
861 construct. Experiment was performed three independent times with similar results. **f**, Time-  
862 dependent labeling of Ser277Cys (background construct: ts2-active, C7X) with MTS-ACMA in  
863 the presence of ibogaine (filled circles) and paroxetine (open squares) in 100 mM NaCl.  
864 Symbols show the mean derived from n=3 technical replicates. Error bars show the s.e.m.  
865 Experiment was performed three times with similar results. **g**, Analysis of Ser277Cys labeling  
866 experiments using MTS-ACMA in the presence of ibogaine or paroxetine analyzed by SDS-  
867 PAGE and visualized by in-gel fluorescence. Experiment was performed three independent  
868 times with similar results. **h**, Three-dimensional reconstruction and fit to the density map with  
869 the model derived from the paroxetine-bound x-ray structure (PDB code: 6AWN)<sup>18</sup>. SERT is  
870 cyan, 15B8 is purple and 8B6 is green; TM1 and TM6 are orange and red, respectively. **i**, The fit  
871 of paroxetine into the EM density map (blue mesh) and interacting residues. **j**, Left panel, details  
872 of the 15B8-SERT interface with the EL2 region shown as an electrostatic surface potential map  
873 and 15B8 shown in ribbon representation. The Fab is colored dark blue (heavy chain) or light  
874 blue (light chain), selected Fab residues within 5 Å of SERT are shown as sticks. The right panel

875 is a similar view but with the Fab shown as a semitransparent electrostatic surface potential.  
876 EL2 of SERT is shown in ribbon representation and colored cyan.

877 **Extended Data Figure 2. Cryo-EM reconstruction of ts2-active 15B8 Fab/8B6**

878 **scFv/paroxetine complex.** **a**, Work-flow of cryo-EM data processing of the ts2-inactive  
879 Fab/scFv complex with paroxetine in outward-open conformation. After particle picking, particles  
880 were sorted using 2D classification. 3D ab-initio classification was performed after 2D  
881 classification on cryoSPARC. One out of two predominant classes (boxed) exhibited a subset of  
882 homogeneous particles which were used for further processing and global alignment in  
883 cryoSPARC. The other class upon refinement only yielded a low-resolution map which did not  
884 exhibit any significant differences upon comparison between classes. cisTEM local refinement  
885 improved the resolution upon masking of the Fab constant domain and micelle (mask is shown  
886 overlaid in blue on top of the reconstruction). The final reconstructed volume was sharpened  
887 using Phenix. **b**, Representative cryo-EM micrograph. Individual single particles are circled in  
888 white. Bar equals 50 nm. **c**, 2D class averages after three rounds of classification. **d**, The  
889 angular distribution of particles used in the final reconstruction. **e**, Cryo-EM density map colored  
890 by local resolution estimation. **f**, FSC curves for cross-validation, the final map (blue), masked  
891 SERT-Fab complex (red), and a mask which isolated SERT (black). The low-resolution limit  
892 cutoff for refinement was 7.5 Å. **g**, model vs. half map 1 (working, red), half map 2 (free, black),  
893 model vs. final map (blue). **h**, Cryo-EM density segments of TM1 - TM12. **i**, A spherical mask  
894 placed over SERT was used for focused 3D classification with 3 classes. Comparison of the  
895 classes did not reveal any substantial differences. The antibodies were removed for clarity. The  
896 number of particles belonging to each class average are: class 1, purple (11.9%, 25,530  
897 particles); class 2, yellow (54.9%, 117,781 particles); class 3, cyan (33.2%, 71,226 particles).

898 **Extended Data Figure 3. Cryo-EM reconstruction of ts2-active 15B8 Fab/8B6 scFv/**  
899 **ibogaine complex.** **a**, Work-flow of cryo-EM data processing of the ts2-active Fab/scFv

900 complex with ibogaine in outward-open conformation. After particle picking, particles were  
901 sorted using 2D classification. Ab-initio was performed in cryoSPARC after 2D classification to  
902 obtain an initial reconstruction. Particles were used for further processing and global alignment  
903 in cryoSPARC followed by recentering in Relion and calculation of the local CTF using GCTF.  
904 cisTEM local refinement improved the resolution upon masking of the Fab constant domain and  
905 micelle (mask is shown overlaid in blue on top of the reconstruction). The final reconstructed  
906 volume was sharpened using cisTEM. **b**, Representative cryo-EM micrograph. Individual single  
907 particles are circled in white. Bar equals 50 nm. **c**, 2D class averages after three rounds of  
908 classification. **d**, The angular distribution of particles used in the final reconstruction. **e**, Cryo-EM  
909 density map colored by local resolution estimation. **f**, FSC curves for cross-validation, the final  
910 map (blue), masked SERT-Fab complex (red), and a mask which isolated SERT (black). The  
911 low-resolution limit cutoff for refinement was 7.5 Å. **g**, Model vs. half map 1 (working, red), half  
912 map 2 (free, black), model vs. final map (blue). **h**, Cryo-EM density segments of TM1 – TM12. **i**,  
913 A spherical mask placed over SERT was used for focused 3D classification with 3 classes.  
914 Comparison of the classes did not reveal any substantial differences. The antibodies were  
915 removed for clarity. The number of particles belonging to each class average are: class 1, purple  
916 (33.6%, 51,739 particles); class 2, yellow (38.8%, 59,747 particles); class 3, cyan (27.6%,  
917 42,500 particles).

918 **Extended Data Figure 4. Cryo-EM reconstruction of ΔN72,C13 SERT/15B8 Fab/ibogaine**  
919 **complex in NaCl. a**, Work-flow of cryo-EM data processing of the ΔN72,C13 SERT/15B8 Fab  
920 complex with ibogaine in occluded conformation. After particle picking, particles were sorted  
921 using 2D classification. Ab-initio was performed in cryoSPARC after 2D classification to obtain  
922 an initial reconstruction. Particles were used for further processing and global alignment in  
923 cryoSPARC followed by recentering in Relion and calculation of the local CTF using GCTF.  
924 cisTEM local refinement improved the resolution upon masking of the Fab constant domain and

925 micelle (mask is shown overlaid in blue on top of the reconstruction). The final reconstructed  
926 volume was sharpened using cisTEM. **b**, Representative cryo-EM micrograph. Individual single  
927 particles are circled in white. Bar equals 50 nm. **c**, 2D class averages after three rounds of  
928 classification. **d**, The angular distribution of particles used in the final reconstruction. **e**, Cryo-EM  
929 density map colored by local resolution estimation. **f**, FSC curves for cross-validation, the final  
930 map (blue), masked SERT-15B8 Fab complex (red), and a mask which isolated SERT (black).  
931 The low-resolution limit cutoff for refinement was 7.0 Å. **g**, model vs. half map 1 (working, red),  
932 half map 2 (free, black), model vs. final map (blue). **h**, Cryo-EM density segments of TM1 -  
933 TM12. **i**, A spherical mask placed over SERT was used for focused 3D classification with 3  
934 classes. Comparison of the classes did not reveal any substantial differences. The Fab was  
935 removed for clarity. The number of particles belonging to each class average are: class 1, purple  
936 (78.9%, 571,547 particles); class 2, yellow (6.9%, 49,983 particles); class 3, cyan (14.2%,  
937 102,863 particles).

938 **Extended Data Figure 5. Cryo-EM reconstruction of ΔN72,C13 SERT/15B8 Fab/ibogaine**  
939 **complex in KCl.** **a**, Work-flow of cryo-EM data processing of the ΔN72,C13 SERT/15B8 Fab  
940 complex with ibogaine in KCl in the inward-open conformation. After particle picking, particles  
941 were sorted using 2D classification. Ab-initio was performed in cryoSPARC after 2D  
942 classification to obtain an initial reconstruction. Particles were further sorted in Relion using 3D  
943 classification and refined further in cryoSPARC. cisTEM local refinement improved the  
944 resolution upon masking of the Fab constant domain and micelle (mask is shown overlaid in  
945 blue on top of the reconstruction). The final reconstructed volume was sharpened using cisTEM.  
946 **b**, Representative cryo-EM micrograph. Individual single particles are circled in white. Bar  
947 equals 50 nm. **c**, 2D class averages after three rounds of classification. **d**, The angular  
948 distribution of particles used in the final reconstruction. **e**, Cryo-EM density map colored by local  
949 resolution estimation. **f**, FSC curves for cross-validation, the final map (blue), masked SERT-

950 Fab complex (red), and a mask which isolated SERT (black). The low-resolution limit cutoff for  
951 refinement was 7.5 Å. **g**, model vs. half map 1 (working, red), half map 2 (free, black), model vs.  
952 final map (blue). **h**, Cryo-EM density segments of TM1 - TM12. **i**, A spherical mask placed over  
953 SERT was used for focused 3D classification with 3 classes. Comparison of the classes did not  
954 reveal any substantial differences. The Fab was removed for clarity. The number of particles  
955 belonging to each class average are: class 1, purple (32.9%, 121,288 particles); class 2, yellow  
956 (33.7%, 124,237 particles); class 3, cyan (33.4%, 123,131 particles).

957 **Extended Data Figure 6. Cholesteryl hemisuccinate, map features at Thr276 and Ser277,**  
958 **and SERT-noribogaine complex. a**, Interaction between CHS, TM1a and TM5 in the occluded  
959 conformation of the  $\Delta$ N72,C13 SERT/15B8/ibogaine complex in 100 mM NaCl. **b**, Non-  
960 proteinaceous density features (red) near Thr276 and Ser277. **c**, Noribogaine inhibition of 5-HT  
961 transport for  $\Delta$ N72,C13 SERT. 5-HT transport was measured using 20  $\mu$ M [ $^3$ H]5-HT in presence  
962 of the indicated concentrations of noribogaine. The mean  $IC_{50}$  of noribogaine inhibition of  
963 serotonin transport was determined from the curve with the error of the fit (s.e.m.):  $1.2 \pm 0.2 \mu$ M.  
964 Symbols show the mean derived from n=3 biological replicates. Error bars show the s.e.m.  
965 Experiment was performed twice independently with the same results. **d**, Michaelis–Menten  
966 plots of 5-HT uptake for the  $\Delta$ N72,C13 transporter in the absence (circles), or in presence  
967 (dash, squares) of 1  $\mu$ M noribogaine, the mean  $K_m$  was determined from the curve with the error  
968 of the fit (s.e.m.):  $\Delta$ N72,C13:  $2.7 \pm 0.6 \mu$ M; in presence of noribogaine:  $2.7 \pm 0.9 \mu$ M. Symbols  
969 show the mean derived from n=3 biological replicates. Error bars show the s.e.m. **e**,  
970 Noribogaine (circles) and ibogaine (dash, squares) competition binding with [ $^3$ H]paroxetine for  
971  $\Delta$ N72,C13 SERT, Symbols show the mean derived from n=3 technical replicates. Error bars  
972 show the s.e.m. **f**, Density map of the  $\Delta$ N72,C13 SERT/15B8/noribogaine complex, in 100 mM  
973 KCl, fit with the model derived from the inward-open ibogaine-bound SERT complex. SERT is  
974 cyan and the 15B8 Fab is purple; TM1 and TM6 of SERT are shown in orange and red,

975 respectively. **g**, Noribogaine density in the central binding pocket. The fit of noribogaine into the  
976 EM density map was derived from ibogaine bound SERT in the inward-open conformation and  
977 shown in blue mesh, and residues involved in binding (Tyr176, Asp98, Phe341, Phe335,  
978 Asn177, Ile172 and Tyr95) are drawn as sticks. **h**, FSC curve for noribogaine bound SERT  
979 complex. The low-resolution limit cutoff for refinement was 9.0 Å.

980 **Extended Data Figure 7. Ibogaine docking and molecular dynamics simulations. a,**  
981 Workflow of ligand docking. **b**, Optimal binding poses of ibogaine in the central binding site of  
982 the outward-open, occluded, and inward-open conformations. For clarity, only TM helices  
983 surrounding the central binding site, i.e., TM1, TM3, TM6, and TM8, are shown. The interaction  
984 between ibogaine and Asp98 of SERT, both shown in sticks, is highlighted. **c**, Simulation system  
985 used to study the structural stability and ibogaine binding of different conformations of SERT  
986 (two independent 50 ns simulations for each conformation), showing the transporter in cartoon,  
987 with 1-palmitoyl-2-oleoyl-sn-glycero-3-phosphocholine lipids drawn in sticks, bulk water in a  
988 transparent surface, and solute ions (100 mM NaCl for the outward-open simulation) in yellow  
989 ( $\text{Na}^+$ ) and green ( $\text{Cl}^-$ ) spheres. **d**, Structural stability of bound ibogaine measured as the mass-  
990 weighted root-mean-square deviation (RMSD, including hydrogen atoms) of the ligand, as well  
991 as the Asp98-ibogaine (O-N) distance. The trajectories of outward-open, occluded, and inward-  
992 open SERT are plotted in red, green, and blue respectively, and shown for two independent  
993 simulations.

994 **Extended Data Figure 8. Measurement of ibogaine and noribogaine inhibition of mutants,**  
995 **effect of thermostabilizing Tyr110Ala mutation, movements of structural elements**  
996 **associated with alternating access mechanism, and alignment of TM5. a**, Inhibition of  
997 serotonin uptake by ibogaine or noribogaine for ts2. The mean  $\text{IC}_{50}$  of ibogaine and noribogaine  
998 inhibition of serotonin transport was determined from the curve with the error of the fit (s.e.m.)  
999 (black circles, ibogaine  $\text{IC}_{50}$ ,  $7 \pm 2 \mu\text{M}$ ; noribogaine  $\text{IC}_{50}$ ,  $1.1 \pm 0.7 \mu\text{M}$ ), Asn177Leu (blue circles,

1000 1 ± 1  $\mu$ M; 40 ± 10  $\mu$ M), Asn177Val (green triangles, 0.17 ± 0.04  $\mu$ M; 24 ± 5  $\mu$ M), Asn177Ala (red  
1001 squares, 0.6 ± 0.3  $\mu$ M; 300 ± 200  $\mu$ M), Asn177Thr (cyan diamonds, 1.0 ± 0.2  $\mu$ M; 8 ± 2  $\mu$ M),  
1002 and Asn177Gln (magenta inverted triangles, 1.1 ± 0.7  $\mu$ M; 1.0 ± 0.5  $\mu$ M). Symbols show the  
1003 mean derived from n=6 and n=3 biological replicates for ibogaine and noribogaine respectively.  
1004 Error bars show the s.e.m. Experiment was performed three times independently with the same  
1005 results. **b**, Comparison of EL4 and TM1b between the x-ray ts3 paroxetine (PDB code: 5I6X,  
1006 purple)<sup>28</sup> structure and the ts2 active ibogaine outward-open cryo-EM structure (grey). Residues  
1007 Tyr110 (ts2-active) and Ala110 (ts3) are shown in sticks. **c**, Comparison of the TM helices of the  
1008 outward-open (grey), occluded (orange), and inward-open (blue) conformations viewed from the  
1009 extracellular side of the membrane. The positions of TM2, 4, 5, and 12 for each conformation  
1010 are shown (middle panel). The right panel shows the helical displacement measured from  
1011 marker positions in each TM to a position in TM3 (Tyr186). Outward-open to occluded  
1012 conformation (filled circles) and from the occluded to the inward-open conformation (open  
1013 circles). The TM marker positions are described further in the 'Methods' section. Error bars  
1014 represent the standard deviation, see Measurement section in Methods for further details. **d**,  
1015 Comparison of the TM helices viewed from the intracellular side of the membrane. The positions  
1016 of TM5, 9, 11, and 12 for each conformation are shown (middle panel). The right panel shows  
1017 the helical displacement measured from marker positions in each TM to a position in TM3  
1018 (Gly160). Outward-open to occluded conformation (filled circles) and from the occluded to the  
1019 inward-open conformation (open circles). Error bars represent the standard deviation. **e**, Angular  
1020 changes of TMs associated with transition from the outward-open to the occluded conformation  
1021 (filled circles) and from the occluded to the inward-open conformation (open circles). Error bars  
1022 represent the standard deviation. **f**, The intracellular region of TM5 'unwinds' in the inward-open  
1023 conformation. Gly278 and Pro288 in the GX<sub>9</sub>P motif are shown in sticks. **g**, Alignment of TM5 of  
1024 SERT, DAT, and NET with LeuT and MhsT. The position of the GX<sub>9</sub>P motif is indicated. **h**,

1025 Comparison of the extracellular loops 3, 4, and 6 in the outward-open (grey), the occluded  
1026 (orange), and the inward-open (blue) conformations.

1027 **Extended Data Figure 9. Comparison of SERT to bacterial transporters.** **a**, Superposition of  
1028 the ibogaine-bound outward-open conformation (light-grey) with the LeuT outward-open  
1029 conformation (PDB code: 3F3A, dark grey)<sup>79</sup>. The graphs depict the RMSD and angular  
1030 differences between the outward-open conformations of SERT and LeuT (3F3A, open triangles),  
1031 LeuT outward-occluded (PDB code: 2A65, open squares)<sup>11</sup>, and LeuT inward-open (PDB code:  
1032 3TT3, closed circles)<sup>8</sup>. **b**, Superposition of the ibogaine-bound occluded conformation (orange)  
1033 with LeuT outward-occluded (PDB code: 2A65, dark grey). The graphs compare the occluded  
1034 conformation of SERT with LeuT conformations as described in **a**. **c**, Superposition of the  
1035 ibogaine-bound inward-open conformation (blue) with LeuT inward-open (PDB code: 3TT3, dark  
1036 grey). The graphs compare the occluded conformation of SERT to LeuT conformations as  
1037 described in **a**. **d**, Comparison of the extracellular loops of LeuT between outward-open (grey),  
1038 occluded (orange), and inward-open (blue) conformations. **e**, Comparison of outward-open  
1039 (light-grey), occluded (orange), and inward-open (blue) with the inward-occluded conformation  
1040 of MhsT (PDB code: 4US3, dark grey)<sup>7</sup>. The graphs compare each conformation of SERT with  
1041 MhsT as described in **a**.

1042 **Extended Data Figure 10. Sodium and chloride ion-binding sites and putative substrate**  
1043 **and ion release pathways.** **a**, Comparison of the Na1 site (green boxes) and the Na2 site  
1044 (purple boxes), and the Cl<sup>-</sup> site (olive boxes) with the outward-open S-citalopram and paroxetine  
1045 x-ray structures of SERT (PDB codes: 5I71 and 5I6X, grey)<sup>28</sup>. Left panel, outward-open ibogaine  
1046 conformation; middle panel, occluded conformation; right panel, inward-open conformation. The  
1047 position of sodium ions found in the x-ray structure are shown in grey. **b**, Solvent accessible  
1048 pathways in the inward-open conformation. Pathway 1 leads from the Na2 site to an opening  
1049 formed between TM1a and TM5. Pathway 2 leads from the central binding site to an opening

1050 between TM1a, TM6b, and TM5. **c**, The minimum radius was plotted as a function of the profile  
1051 of the pathway. The radius of the bicyclic amine moiety of ibogaine is approximately 2.5 Å.

1052

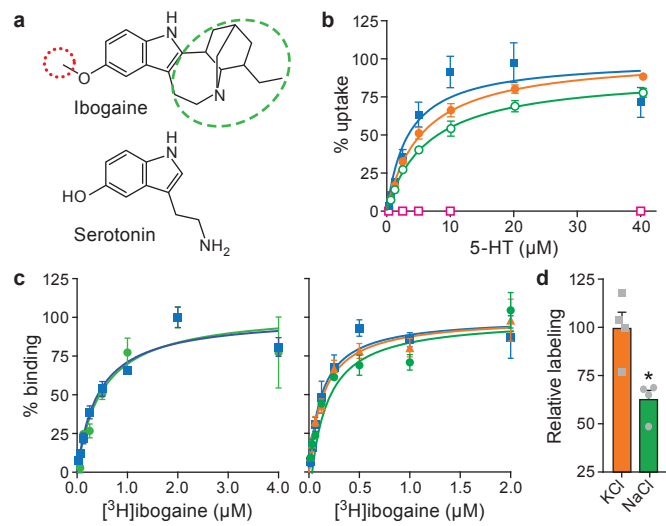


Figure 1

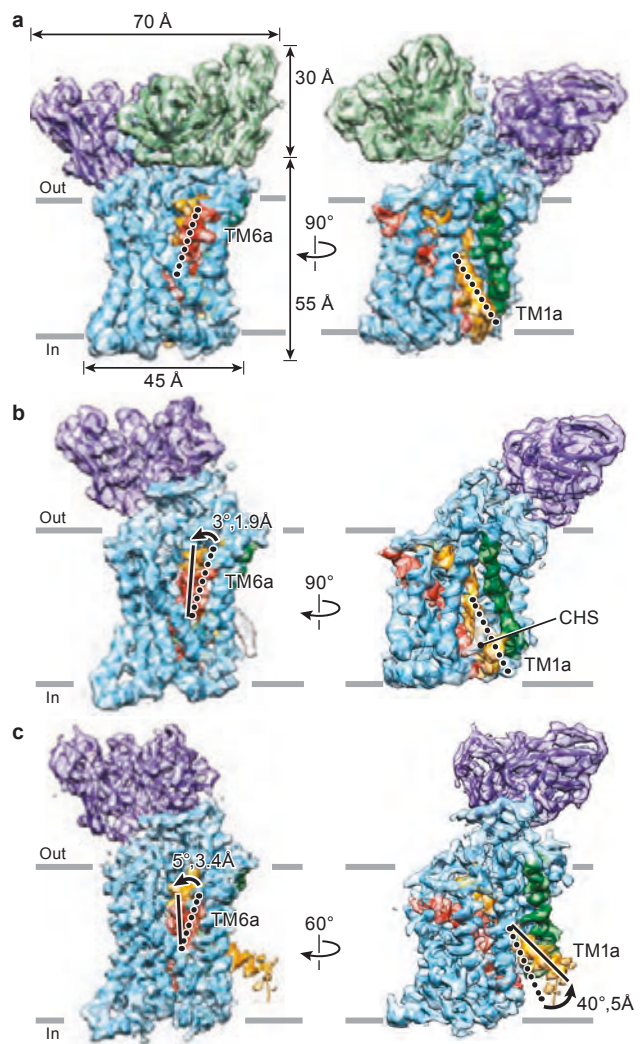


Figure 2

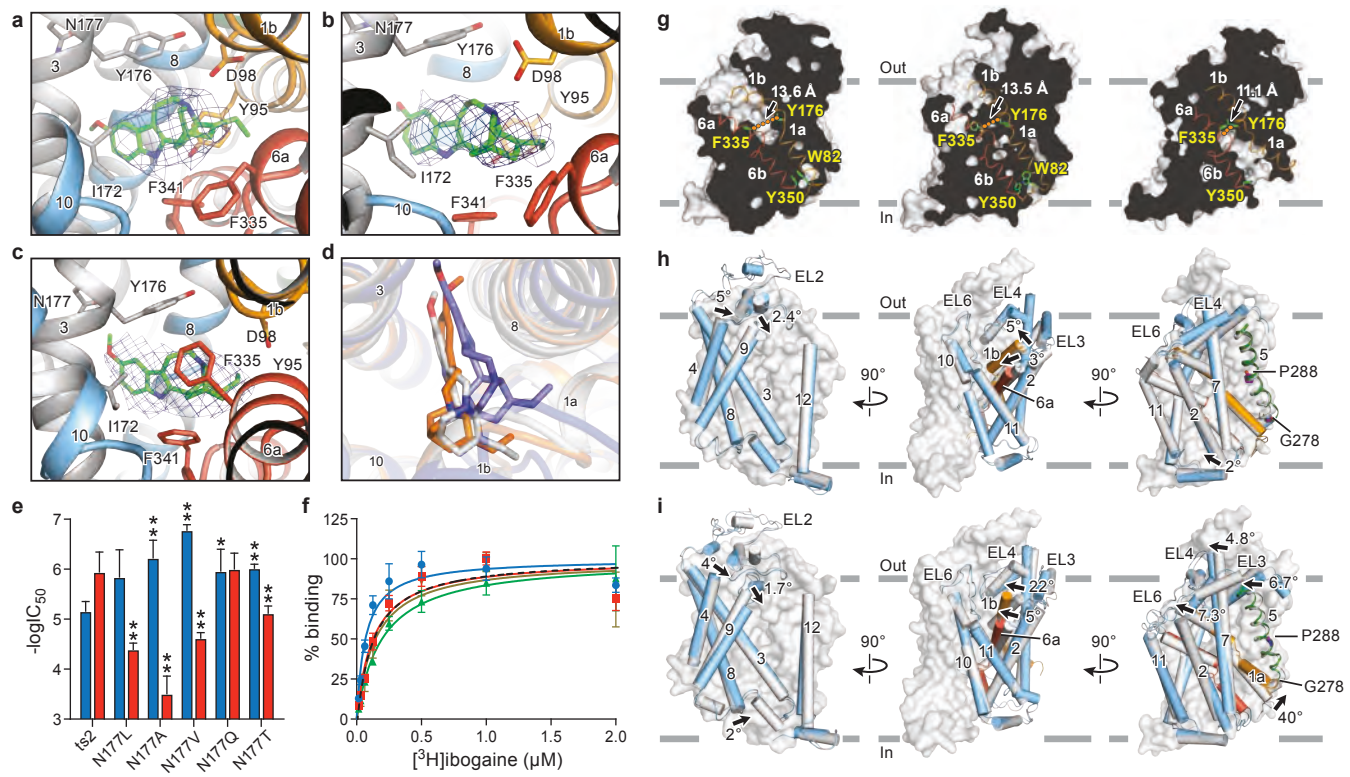


Figure 3

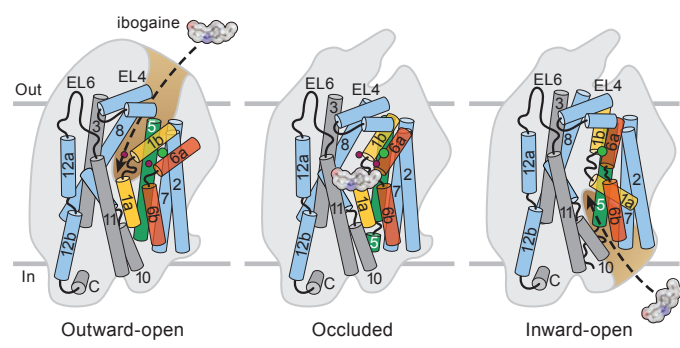


Figure 4